Journal of Inorganic Biochemistry 199 (2019) 110769

Contents lists available at ScienceDirect

Journal of Inorganic Biochemistry

journal homepage: www.elsevier.com/locate/jinorgbio

Modulation of ruthenium anticancer drugs analogs with tolfenamic acid: Reactivity, biological interactions and growth inhibition of yeast cell

Priyaranjan Kumar[a], Swati Swagatika[b], Srikanth Dasari[a], Raghuvir Singh Tomar[b], Ashis K. Patra[a,*]

[a] Department of Chemistry, Indian Institute of Technology Kanpur, Kanpur 208016, Uttar Pradesh, India
[b] Laboratory of Chromatin Biology, Department of Biological Sciences, Indian Institute of Science Education and Research (IISER), Bhopal 462066, India

ARTICLE INFO

Keywords:
Medicinal inorganic chemistry
Ruthenium
NSAID
Crystal structure
Yeast cells
Mitochondrial toxicants

ABSTRACT

We synthesized two ruthenium(II) complexes: *trans*,*trans*-[Ru(im)$_2$(tfa)$_2$] (**1**) and *trans*,*trans*-[Ru(in)$_2$(tfa)$_2$] (**2**) where im = 1*H*-imidazole, in = 1*H*-indazole and tfa = tolfenamic acid, a potential nonsteroidal anti-inflammatory drug (NSAID). The NSAID was opted as bioactive ligand to understand its synergistic therapeutic effect in structurally analogous Ru(II)-compounds with KP418 (imidazolium *trans*-[tetrachloridobis(1*H*-imidazole)ruthenate(III)]) and KP1019 (indazolium *trans*-[tetrachloridobis(1*H*-indazole)ruthenate(III)]). The complexes were studied using various analytical methods and structure was determined by X-ray crystallography. Both the complexes display discrete mononuclear Ru(II) center in {RuN$_4$O$_2$} distorted octahedral geometry. The reactivity of the complexes was tested with potentially important biomolecules involved in metabolism of cancer cells, viz. L-arginine, DL-methionine, glutathione and L(+)ascorbate. Such studies intended to provide deeper insights on intracellular speciation and kinetic substitution encountered by Ru-drugs to target alternative cell death pathways. The complexes demonstrate a preferential binding affinity with calf thymus DNA ($K_b \sim 10^4\ M^{-1}$) and human serum albumin ($K_{HSA} = 10^5\ M^{-1}$). Both the complexes showed potent inhibition of wild type yeast cell growth in a dose-dependent manner. Yeast cells were used as a powerful model system to study the molecular mechanism of pathobiology which shares a high degree of conservation of both cellular and molecular processes with human cells for assessing toxicity potential of the complexes. Fluorescence imaging studies reveal the localization of both complexes to yeast mitochondria despite its rigid cell wall and induce mitochondrial damage and formation of reactive oxygen species (ROS). The Micrococcal nuclease assay revealed complexes do not alter global nucleosome occupancy and probably target specific regions of the genome.

1. Introduction

Cancer is a global burden and leading cause of millions of deaths per year and combating it is an uphill task with high mortality and narrow range of possible clinical use [1]. Although ~200 anticancer drugs are presently available in the clinic, many of them are either ineffective or develop drug-resistance at advanced stages with severe side effects. The limitation in understanding the complex carcinogenesis pathways at the molecular level is a big challenge towards personalized or precision anticancer medicine. In chemotherapy, the platins (*cis*platin, carboplatin, oxaliplatin) have reached a milestone for treating various types of cancers as the first line of defense. However, all these Pt(II) drugs ultimately showed dose-dependent limitations and off-target side effects due to their significant toxicities and acquired drug resistance [2]. Current efforts are towards designing kinetically stable octahedral platinum(IV) prodrugs, where additional axial ligands can be utilized further for targeted delivery utilizing site-specific cancer cell biomarkers compared to healthy cells. However, till now, no significant alternative of platins that can circumvent limitations of drug resistance, associated toxic side effects, and applicability towards a wide range of tumor types was discovered [3–5]. In light of discovery on cell-death pathways and relevant hallmarks of cancers in the post-genomic era, the direction should shift in search of new biological targets and targeting alternative hallmarks of cancer.

Ruthenium complexes have attracted increasing interest in the last two decades as a new generation of metallodrugs. Ruthenium antimetastatic drug NAMI-A (imidazolium *trans*-[tetrachlorido(1*H*-imidazole)(*S*-dimethyl sulfoxide)ruthenate(III)]), developed by G.

* Corresponding author.
E-mail addresses: rst@iiserb.ac.in (R.S. Tomar), akpatra@iitk.ac.in (A.K. Patra).

https://doi.org/10.1016/j.jinorgbio.2019.110769
Received 8 January 2019; Received in revised form 5 July 2019; Accepted 10 July 2019
Available online 11 July 2019
0162-0134/ © 2019 Elsevier Inc. All rights reserved.

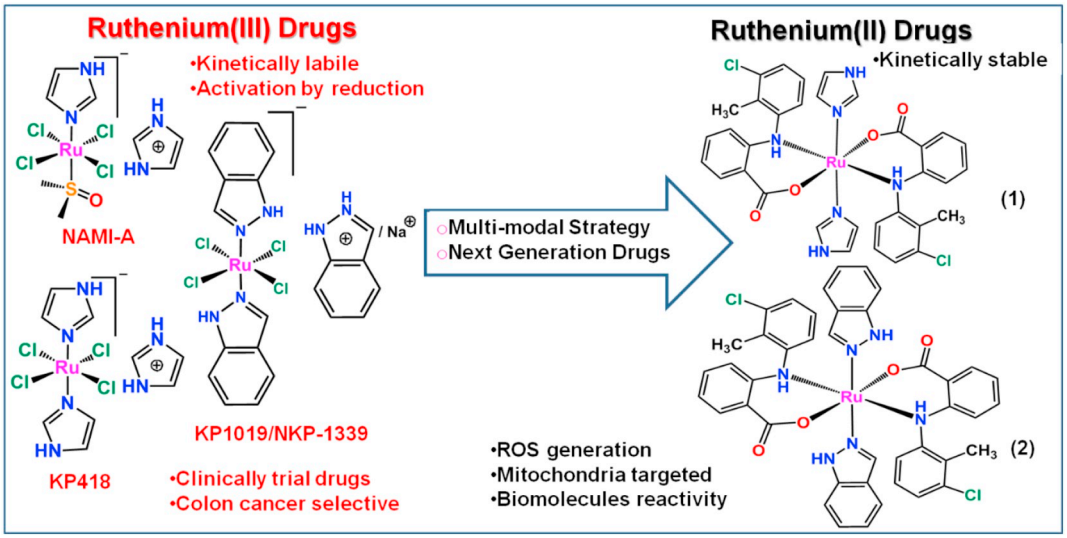

Fig. 1. Schematic representation of current ruthenium(III) NAMI-A and KP/NKP drugs (left) and our designed complexes *trans*,*trans*-[Ru(im)$_2$(tfa)$_2$] (**1**) and *trans*,*trans*-[Ru(in)$_2$(tfa)$_2$] (**2**) (right) where, tfa is tolfenamic acid (NSAID), im = 1*H*-imidazole, in = 1*H*-indazole. (For interpretation of the references to color in this figure, the reader is referred to the web version of this article.)

Sava and E. Alessio and a series of anticancer drugs, viz. KP418 (imidazolium *trans*-[tetrachloridobis(1*H*-imidazole)ruthenate(III)]) and KP1019 (indazolium *trans*-[tetrachloridobis(1*H*-indazole)ruthenate (III)]), or NKP1339 (sodium *trans*-[tetrachloridobis(1*H*-indazole)ruthenate(III)]) introduced by B. K. Keppler and co-workers, are already reported to have excellent therapeutic activity (Fig. 1) [6–13]. Interestingly, NAMI-A, KP1019, and NKP1019 have reached for clinical trials, and their success in initial phases is promising. Although, clinical investigation of NAMI-A remained disappointing and it is no longer in clinical trials, however lesson obtained were provoking chemists to develop new generation ruthenium drugs with enhanced efficacy and selectivity towards specific hallmarks of cancers [14,15]. The underlying mechanisms of drug action facilitate its tumor cell selectivity and less toxicity over platinum drugs [12,16]. The NAMI-A primarily inhibits lung metastasis and show synergism in combination with cisplatin (*cis*-diamminedichloridoplatinum(II)), gemcitabine (2′-deoxy-2′,2′-difluorocytidine), taxanes (paclitaxel, docetaxel), and doxorubicin. The precise metastatic inhibition by NAMI-A is attributed to its ability to cause cell cycle arrest at G2/M phase (growth/mitotic phases), actin dependent adhesion, inhibition of erk1/2 (extracellular-signal regulated kinase), activation of c-myc (an oncogene protein which code for transcription facotors), which promotes the fibrotic reaction and collagen binding [17–20].

KP418, a structurally similar drug of NAMI-A, showed significant activity against colorectal cancer [21]. Anticancer activity and apoptosis-related to the KP1019 and NKP-1339 arise from an array of biological targets, like DNA, strong binding affinity to serum and transferrin or generation of reactive oxygen species (ROS) which consequently lead to mitochondrial damage, G_2/M cell cycle arrest and activation of mitogen-activated protein kinase (MAPK) p38 [12,22,23].

Apart from classical Ru(III) antimetastatic NAMI-A and anticancer KPs, several organometallic arene Ru(II) complexes are gaining increasing interests for their remarkable therapeutic activity in recent years. For example, [(η^6-biphenyl)Ru(en)Cl]$^+$ (en = ethylenediamine) (RM175) and an extensive series of RAPTA complexes [η^6-arene)Ru(PTA)Cl$_2$]$^+$ (PTA = 1,3,5-triaza-7-phosphaadamentane) (RAPTA-A/B/C/T) and [Ru(phenanthroline)(κ-*C*,*N*-(2-phenyl-pyridine)(NCMe)$_2$]PF$_6$ (RDC11) are well-known Ru(II) complexes that do not follow conventional activation by reduction mechanism and shows promising anticancer activities with reduced side effects. Although several Ru(II) drugs target DNA in a fashion different from *cis*platin, they also target many other hallmarks of cancer and show non-cross resistance with the platin drugs. The distinct pharmacological properties and reactivity of Ru^{II} vs Ru^{III} complexes intrigued us to develop new generation of Ru(II) metallodrugs using synergistic bioactive non-steroidal anti-inflammatory drugs (NSAID) ligands [24–30].

NSAIDs are currently gaining more interest in cancer chemoprevention for various aggressive solid tumors [31–33]. NSAIDs are employed in the development of combinatory anticancer agents in synergism with platinum-based drugs [34,35]. Metal-bound NSAID drugs are proven more potent than their free form [36,37]. Synergism in combination with antitumor drugs arises by inhibition of cyclooxygenase (COX) mediated prostaglandins production. The COX inhibition is capable of inducing apoptotic cell death by NSAIDs activated gene-1 overexpression and via transforming growth factor-β (TGF-β) expression [38,39]. Anthranilic acid based NSAIDs (e.g. tolfenamic acid) are also known to affect the mitochondrial permeability [40].

Herein, our strategy is based on designing targeted Ru(II)-based anticancer drugs via conjugating a secondary biologically active ligand tolfenamic acid (tfa) as structural analogs of Ru(III)-drugs like KP-1019/418. We synthesized two Ru(II) complexes: *trans*,*trans*-[Ru(im)$_2$(tfa)$_2$] (**1**) and *trans*,*trans*-[Ru(in)$_2$(tfa)$_2$] (**2**) where im = 1*H*-imidazole, in = 1*H*-indazole (Fig. 1). This design strategy may render resulting compounds with different pharmacological targets in cell-death pathways or alteration in multi-drug resistance. We report here synthesis, structures, encounters with metabolically relevant biomolecules and biological targets, DNA and human serum albumin (HSA). We used rather unconventional yeast cells as a model system to access the toxicity and mechanistic aspects, considering that it shares a great extent of conservation of cellular and molecular mechanism with human cells and could be extrapolated to the cancer cell lines [41–45]. The cytotoxicity was studied by yeast cell growth inhibition. The subcellular localization studied by fluorescence imaging, and mitochondrial function impairment through reactive oxygen species (ROS) generation. The micrococcal nuclease assay (MNase) used to evaluate alteration in global chromatin architecture in yeast cells.

2. Result and discussion

2.1. General physicochemical aspects

[Ru(im/in)$_2$(tfa)$_2$] (**1**, **2**) were synthesized in good yield by refluxing imidazole or indazole with [Ru(DMSO)$_4$Cl$_2$] in ethanol followed by further ligation with neutralized tolfenamic acid (tfa). The identity

Table 1
Selected physicochemical data complexes **1** and **2**.

Complex	IR[a]/cm^{-1} $\nu_{as(COO)^-}$	$\nu_{s(COO)^-}$	$\Delta\nu$/cm^{-1}	λ_{max}[b]/nm, (ε/M^{-1} cm^{-1})	τ[c](ns)
1	1579	1377	202	300(23770), 480(2970), 738(4690)	2.70
2	1581	1372	209	290(28410), 509(1660), 741(1220)	5.93

[a] In KBr phase.
[b] UV-visible spectra in DMF.
[c] Decay lifetime in DMF.

and purity of the compounds were confirmed by elemental analysis, ESI-MS, ^{1}H NMR, FT-IR, UV–vis, electrochemistry and fluorescence spectroscopy. Both the complexes were structurally characterized using single crystal X-ray crystallography. Physicochemical data for both the complexes is shown in Table 1. ESI-MS analyses for **1** and **2** shows respective molecular ion peaks, [M-H]$^+$ at m/z = 757.07 and [M + H]$^+$ at m/z = 859.10 (Fig. S1). Upon binding with Ru(II), FT-IR bands corresponding to 3355 cm^{-1} ($\nu_{O\text{-}H}$) disappears and shifting of ν_{as} and ν_s for free carboxylic (−COOH) group is observed. The complexes show $\nu_{as(COO)^-}$ at ~1580 cm^{-1} and $\nu_{s(COO)^-}$ at 1377 cm^{-1} (**1**) and 1372 cm^{-1} (**2**) (Table 1 and Fig. S2). The difference of asymmetric and symmetric mode of stretching for complexes **1** and **2** ($\Delta\nu$/cm^{-1}) are 202 and 209 cm^{-1}, which confirms monodentate carboxylate binding to Ru(II) centers [46]. ^{1}H NMR of complexes **1** and **2** showed no signal corresponding to −COOH group indicating complexation of tfa ligand to Ru (II) after deprotonation (Figs. S3 and S4). The characteristic NH proton of imidazole and indazole showed upfield shift compared with the free ligand, while NH proton of tolfenamic group shifted downfield in ^{1}H NMR spectra. The downfield shift of NH proton signal of tfa is attributed to coordination to the Ru(II) [47–49]. Interestingly, the signal corresponding to CH_3 was observed at 2.29 (**1**) and 2.26 ppm (**2**). Complexes show strong absorption maxima band in DMF at 300 nm (23,770 M^{-1} cm^{-1}) and 290 nm (28,410 M^{-1} cm^{-1}) for complex **1** and complex **2** respectively, which corresponds to π-π* transitions of tolfenamic acid (Fig. 2(a)) [50]. A broad absorption band in electronic spectrum around 400–575 nm and 400–600 nm arises from Ru(dπ) → (^{1}MLCT) for complex **1** and **2** respectively. A distinct low energy band in electronic spectra centered ~740 nm was also observed.

Time-dependent ^{1}H NMR spectra showed no apparent spectral changes in ^{1}H peak position in DMSO-d_6 (Figs. S5 and S6). Similarly, absorption spectral analyses for both the complexes in DMF and DMSO showed no significant changes in absorptions spectral traces at 298 K with time (Figs. S7 and S8). The time-dependent ^{1}H NMR, absorption spectra, and ESI-MS analysis strongly suggest the stability of the octahedral Ru(II) complexes in solution. The ^{1}H NMR of compounds **1** and **2** recorded at 333 K showed only peak broadening for im/in −NH proton (proton 'b' for **1** and proton 'a' for **2**) and seem thermodynamically stable in solution (Figs. S9 and S10). Both the complexes show metal-based broad emission centered at 510 nm (**1**) and at 410 nm (**2**) (λ_{exc} = 325 nm) (Fig. 2(c)). Excitation spectra for complexes recorded in DMF at 298 K with emission at 550 nm show a broad band at ~312 nm (Fig. S11) due to π-π* transitions of the bound tfa$^-$ ligand. Upon excitation with low energy absorption band of 480 nm, complex **1** displays two emission bands at 515 nm and 555 nm, whereas complex **2** at λ_{ex} = 505 nm, exhibit similar emissions at λ_{em} = 530 nm and 553 nm (Fig. S12). The average lifetime measured for decay at 510 nm and 410 nm for complexes **1** and **2** are 2.70 ns and 5.93 ns respectively (using Eq. (1)) with λ_{ex} = 340 nm in DMF at 298 K (Fig. 2(d) [51,52]. Both the complexes were redox-active and showed an irreversible oxidative $Ru^{II/III}$ couple at 1.21 V and 1.20 V vs Ag/AgCl for **1** and **2** respectively (Figs. 2(b), S13). Oxidative (Ru^{II}/Ru^{III}) redox values are in agreement with values reported for similar Ru^{II} complexes [53].

2.2. Crystal structure

The complexes *trans*,*trans*-[Ru(im)$_2$(tfa)$_2$] (**1**) and *trans*,*trans*-[Ru(in)$_2$(tfa)$_2$] (**2**)·2CHCl$_3$ crystallizes in triclinic *P*-1 space group. The structure of the complexes was distorted octahedral with {RuN_4O_2} core two oxygens and two nitrogens from two tolfenamic acid and two nitrogens from two imidazoles/indazoles in *trans* orientation. The asymmetric unit of both complex structures contains one half of the molecule with Ru-centre at a special position with site occupancy factor (SOF) of 0.5 (i.e. 50% occupancy). An ORTEP view of the structures of complexes is shown in Fig. 3 and the details of crystallographic refinement parameters are shown in Table S1. The unit cell packing diagrams and the bond lengths and bond angles are given in Fig. S14 and Table S2. The unit cell of **1** contains a single molecule of complex whereas **2** crystallizes with two $CHCl_3$ solvent molecules.

The bond lengths of Ru-N/O vary from 1.957(2) to 2.081(2) Å (**1**) and 1.968(3) to 2.063(3) Å (**2**) and are in the range of literature reported values for analogous complexes [54–56]. The bond angles constituting octahedral core varies from 86.39(9)° to 93.61(9)° (**1**) and 86.50(9)° to 93.50(9)° (**2**). The bite angles of two tolfenamic acids are different: ∠N(3)-Ru(1)-O(1) = 86.39(9)° (for **1**) and 86.50(9)° (for **2**) respectively. The [im-Ru-im] or [in-Ru-in] planes are perfectly axially coplanar and these planes are nearly perpendicular to [tfa-Ru-tfa] planes with dihedral angle of 88.89° and 88.51° respectively for **1** and **2** (Fig. S15). In 3D crystal lattice, they exhibit weak intermolecular π-π interactions at a distance 3.948 Å (**1**) and 3.987 Å (**2**) between two aromatic rings of tfa ligands of neighboring molecules (Fig. S16). The complexes also exhibit possible intermolecular hydrogen bonding between NH(im)…O(tfa) at1.837 Å (**1**) atoms and NH(in)…O(tfa) at 1.993 Å (**2**) (Fig. S17).

2.3. Interaction with L-arginine, DL-methionine, GSH and L(+) ascorbate

Administration of any drug in cell encounters numerous interactions and possible reactions with several molecules before reaching its intended biological target; therefore, it is very important aspect to understand their fate or mechanism of action in situ. A tumor cell always in demand of high-energy programming processes for its survival, rapid proliferation and viability. The metabolic alteration makes them vulnerable on exogenous nutrient sources like amino acids. This pathological condition provides several biomarkers and opportunities for therapeutic intervention, selective targeting, and prognosis, and metabolic imbalance thus considered as one of the principal hallmarks of cancer [57,58]. Therefore, it is very important to understand these underlying reactions to realize the full potential of a new therapeutic drug with possibly lower drug-resistance. In this context, here we have tested compounds **1** and **2** with few potentially interacting biochemicals.

The L-arginine auxotrophy (depletion of L-arg), is a characteristic of several cancer types, has been elegantly utilized, and arginine deprivation was investigated as novel metabolic anticancer therapeutic strategy induced by prolonged endoplasmic reticulum (ER) stress [59–61]. Methionine is involved in protein synthesis, DNA methylation, and as a glutathione (GSH) precursor and methionine restriction to cancer cells regarded as a chemotherapeutic intervention for cancer [62,63]. GSH functions as an antioxidant and protects cells from damage caused by free radicals, peroxide and toxic agents including cytotoxic drugs. GSH forms adduct with drugs and effluxes out from the cell leading to drug deactivation, therefore, modulation of cellular GSH level proven to overcome drug-resistance and enhanced chemo-sensitization [64–66]. The combination of vitamin C with NSAIDs (Sulindac) is found to be potent in human colon cancer with p-53 (a tumor suppressor protein), and ROS mediated apoptosis, and synergism with a chemotherapeutic drug like doxorubicin, cisplatin and paclitaxel is well-established [67,68].

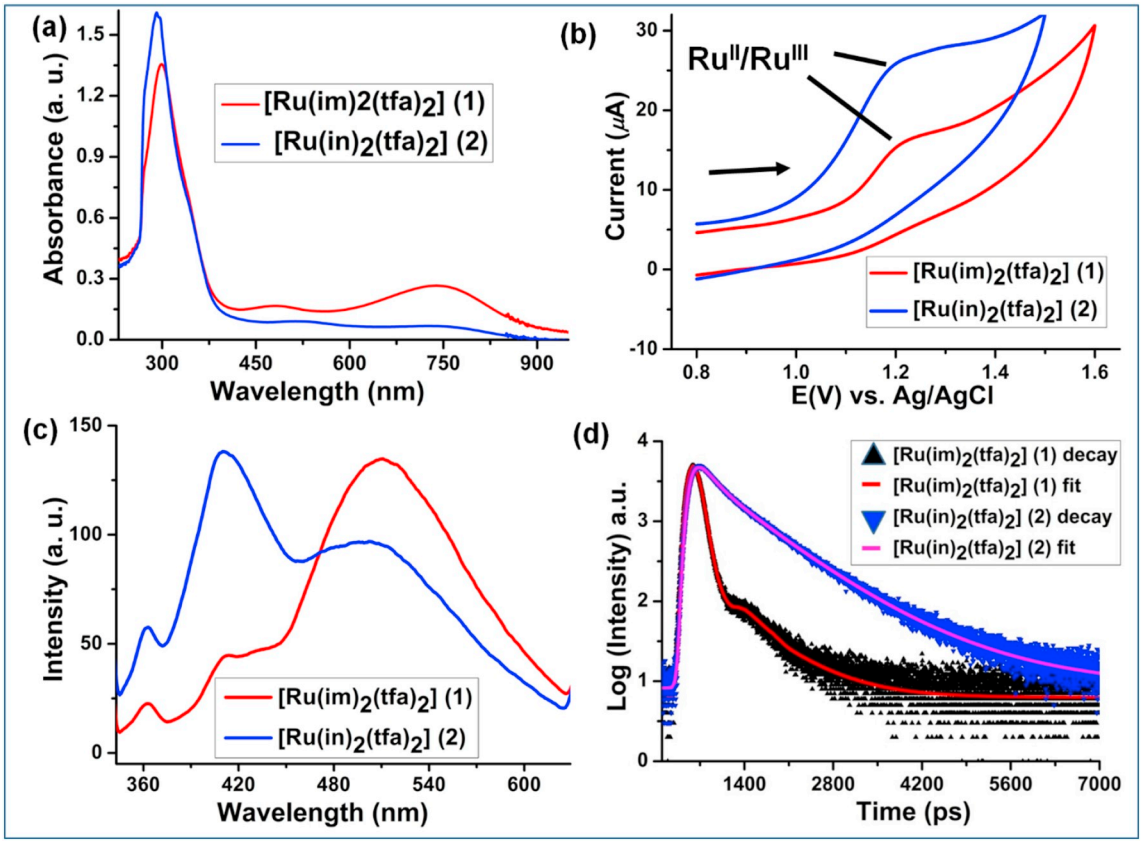

Fig. 2. Photophysical and electrochemical properties of complexes **1** and **2**: (a) UV–vis electronic absorption spectra for complex **1** and **2** (48 μM) in DMF at 298 K. (b) Cyclic voltammograms of complexes **1** and **2** (1 mM) at 298 K with 0.1 M TBAP (tetrabutylammonium perchlorate) as supporting electrolyte in DMF at a scan speed of 100 mVs^{-1} representing Ru^{II}/Ru^{III} redox couple. (c) Emission spectra of complex **1** (29 μM) and **2** (10 μM) in DMF at 298 K, λ_{exc} = 325 nm and excitation and emission slit width 10 nm. (d) Fluorescence lifetime decay curve and fit for complexes **1** (510 nm) and **2** (410 nm) in DMF using λ_{exc} = 340 nm. (For interpretation of the references to color in this figure, the reader is referred to the web version of this article.)

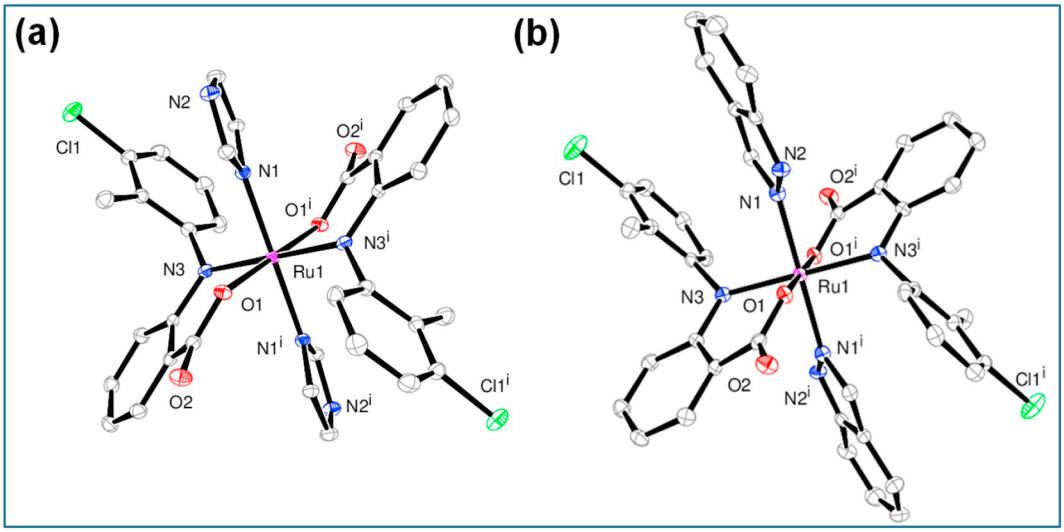

Fig. 3. ORTEP views with 50% probability thermal ellipsoids and numbering scheme for metal and heteroatoms: (a) *trans,trans*-$[Ru(im)_2(tfa)_2]$ (**1**). Selected bond distances: Ru(1)-N(1), 2.081(2) Å; Ru(1)-N(3), 1.957(2)Å; Ru(1)-O(1), 2.038(2) Å. (b) *trans,trans*-$[Ru(in)_2(tfa)_2]$ (**2**)·$2CHCl_3$. Selected bond distances: Ru(1)-N(1), 2.063(3) Å; Ru(1)-N(3), 1.968(3) Å; Ru(1)-O(1), 2.028(2) Å. The solvent molecules and hydrogen atoms were removed for clarity.

Herein, the complexes were incubated with excess of L-arginine (0–1100 μM for **1** and 0–1261 μM for complex **2**), DL-methionine (0–930 μM for **1** and 0–909 μM for **2**), GSH (0–296 μM for **1** and 0–470 μM for **2**) and sodium ascorbate (0–935 μM for **1** and 0–1091 μM for **2**). The reactions were monitored spectroscopically from a change in emission profile of complexes in mixture of DMF and tris-HCl-NaCl buffer under physiological pH and further analyzed by ESI-MS. A continuous decrease in emission intensity at 510 nm was observed upon encounter of an excess of L-arginine, DL-methionine and GSH, however, with L(+) ascorbate, it shows non-significant changes at

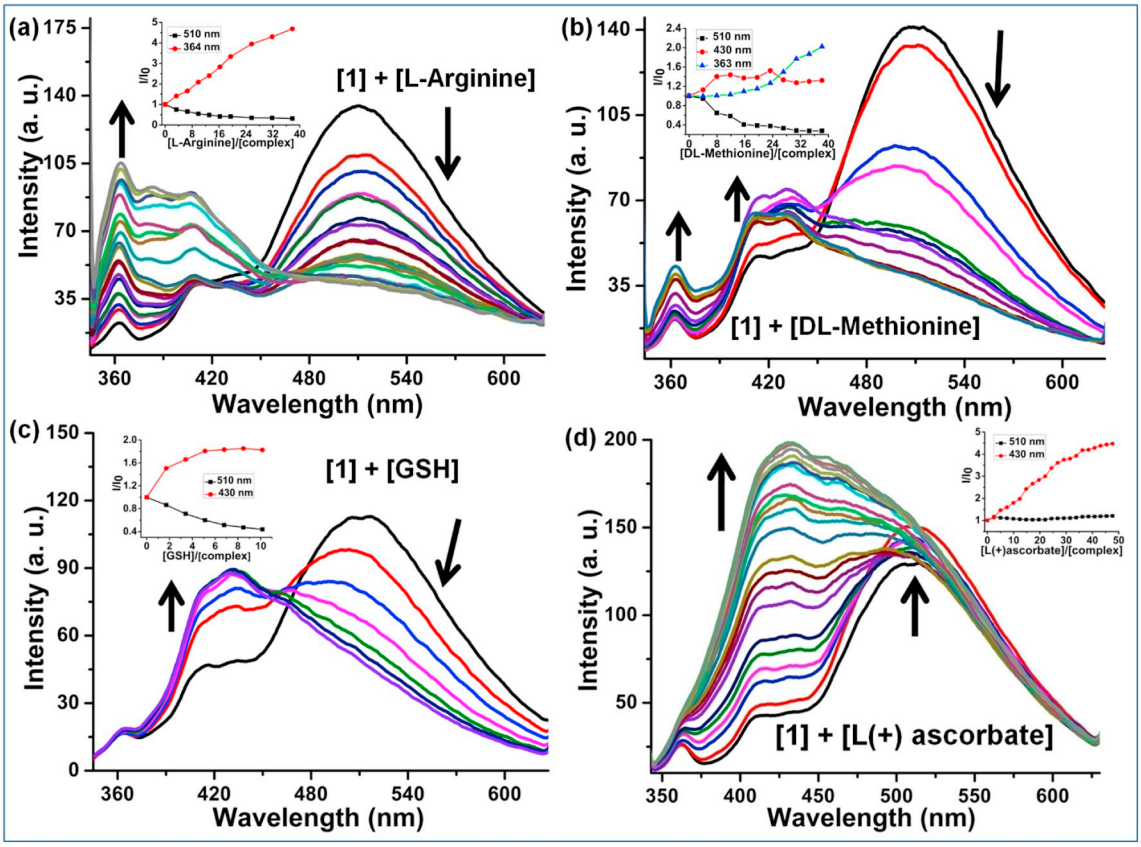

Fig. 4. Evolution of emission spectra of complex **1** upon titration with excess of biomolecules; L-arginine, DL-methionine, GSH and L(+) ascorbate and arrow gives the direction of change in emission profile measured in DMF-Tris-HCl/NaCl buffer (pH = 7.2) mixture at 298 K with λ_{exc} = 325 nm. (a) **1** (29 μM) with L-arginine (0–1100 μM) in DMF-buffer (50:3). Inset: variation of relative changes of intensity (I/I_0) with [L-arginine]/[complex] at 510 nm and 364 nm. (b) **1** (24 μM) with DL-methionine (0–930 μM) in DMF-buffer (20:1). Inset: variation of relative changes of intensity (I/I_0) with [DL-methionine]/[complex] at 510 nm, 430 nm and 363 nm. (c) **1** (29 μM) with reduced glutathione (GSH) (0–296 μM) in DMF-buffer (200:3). Inset: variation of relative changes of intensity (I/I_0) with [GSH]/[complex] at 510 nm and 430 nm. (d) **1** (20 μM) with L(+) ascorbate (0–935 μM) in DMF-buffer (20:1). Inset: variation of relative changes of intensity (I/I_0) with [L(+) ascorbate]/[complex] at 510 nm and 430 nm. (For interpretation of the references to color in this figure, the reader is referred to the web version of this article.)

λ_{em} = 510 nm. The decrease in intensity at 510 nm upon addition of biomolecules also show a simultaneous increase in intensity at 364 nm for L-arginine and DL-methionine and at 430 nm for both GSH and ascorbate for complex **1** (Fig. 4). The complex **2** also showed a simultaneous increase in intensity at 364 nm, 415 nm, and 430 nm upon the respective addition of these compounds (Fig. S18). The abrupt spectral changes and formation of new emission bands indicate the formation of a new Ru-species, possibly via ligand substitution reactions. Further, the time-dependent emission spectral traces of titrated samples do not show appearance of any new bands up to 4 h, indicating kinetic stability of the product in the solution and irreversible mode of binding with these biomolecules (Figs. S19 and S20). ESI-MS analysis of the reaction mixtures shows the formation of covalent adducts with complex **1** (Fig. 5, Fig. S22). The results suggest that complexes are more susceptible to substitution reaction with GSH compared to L-arginine, DL-methionine, and L(+) ascorbate. Such reactivity studies may provide an insight into the possible exact intracellular speciation, the identity of active species, ligand substitution kinetics, and mechanism of cell death. The covalent adducts with L-arginine, DL-methionine corresponds to possible arginine deprivation and methionine restriction, which could be utilized as a new modality of treatment of threatening tumor types that rely on these biomolecules for its proliferation.

2.4. DNA binding studies

2.4.1. Absorption spectral studies

The DNA binding is the crucial step in action of several FDA approved anticancer platins [69] and organic drugs such as doxorubicin, gemcitabine, 5-fluorouracil, etc. Several ruthenium-polypyridyl complexes have been explored for their unique properties of covalent and non-covalent binding with DNA and also as molecular light switch, charge transporter and metallo-intercalators [70,71]. DNA binding measurements provide mechanistic insight into mode of action of drugs. The measurement of binding affinity of complexes to DNA was performed by absorption spectral methods, which shows a significant hypochromism and red-shift in their electronic absorption spectra [72]. Results obtained from DNA binding experiment is shown in Figs. 6(a) and S23. Hypochromism of tolfenamic acid based лπ–π* absorption bands at 290 nm for complex **1** and 295 nm for complex **2** was observed upon increasing amount of CT–DNA (0–65 μM for **1** and 0–48 μM for **2**) to the metal complex solution. The equilibrium binding constant (K_b) determined affinity to DNA for both complexes and obtained from the ratio of the slope to the intercept of a half-reciprocal plot using Eq. (2) and listed in Table 2. The DNA binding constant values for the complexes **1** $(5.87 \pm 0.3) \times 10^3$ < **2** $(2.10 \pm 0.13) \times 10^4$, possibly due to effective intercalation from extended conjugation of indazole (**2**) than imidazole (**1**).

2.4.2. Ethidium bromide displacement assay

Ethidium bromide displacement assay was performed to evaluate the competitive binding capability of complexes with duplex DNA. In the absence of DNA, EthB does not show any significant emission in buffer medium, while in presence of DNA, the emission intensity gets enhanced and hence used as an emissive spectral probe for DNA

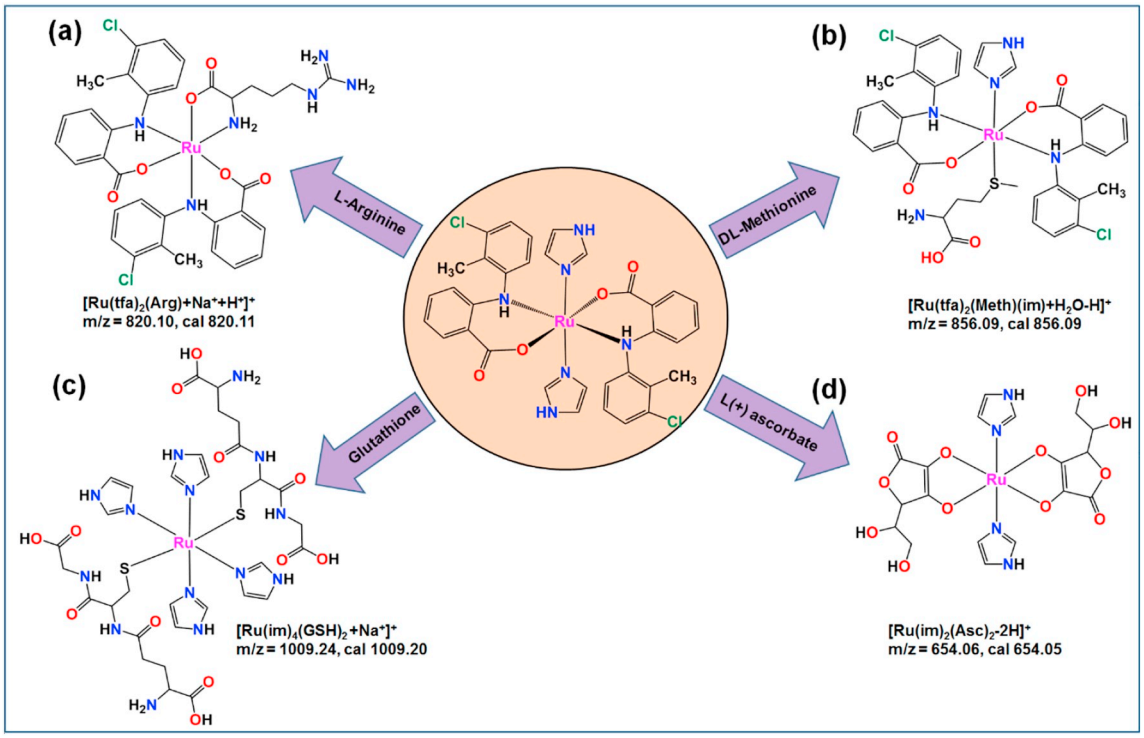

Fig. 5. Reactivity profile of complex **1** after encounter with an excess of biomolecules; (a) L-arginine, (b) DL-methionine, (c) reduced glutathione, and (d) L(+) ascorbate showing the formation of various adducts as determined from ESI-MS in a mixture of DMF and 5 mM Tris-HCl/NaCl, pH 7.2 buffer. (For interpretation of the references to color in this figure, the reader is referred to the web version of this article.)

binding [73]. The gradual addition of complexes to luminescent EthB (12 μM)-DNA (6.4 μM) adduct leads to displacement of bound EthB and consequent quenching in emission intensity at 603 nm (λ_{exc} = 546 nm) (Figs. 6(b) and S24). Apparent DNA binding constants were calculated from Eq. (3) and listed in Table 2. The higher K_{app} values of 10^6 M^{-1} for both the complexes are indicative of better intercalation ability for both the complexes [74,75].

2.5. Protein binding studies

2.5.1. Human serum albumin (HSA) binding interactions

Serum albumin is a class of multigene protein and plays a vital role in the control of osmotic blood pressure and help in transport, distribution, and metabolism of several endogenous and exogenous compounds [76]. Studying the binding interaction of drugs with human serum albumin (HSA) can determine pharmacokinetic and pharmacodynamic properties. HSA is made up of non-glycosylated polypeptide having 585 amino acids with three structurally similar domains and each domain having two subdomains providing overall heart-shaped structure. Subdomains IIA and IIIA are principal hydrophobic binding regions of HSA for drug or ligand binding viz. Digitoxin, ibuprofen while warfarin binds in IIA subdomain. Emission spectral properties of HSA arise from the presence of tryptophan, tyrosine and phenylalanine residues [77]. The change in emission intensity of tryptophan residue in the presence of tested compound is therefore used as a spectral probe to measure its binding affinities with HSA. Binding interactions of both the

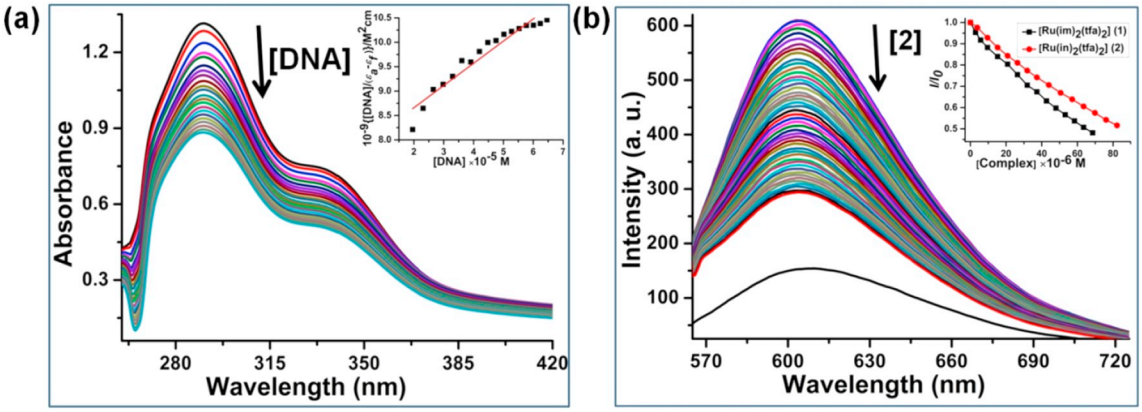

Fig. 6. (a) Absorption spectral traces of complex **1** (70 μM) in in the presence of increasing CT-DNA (0–65 μM) concentrations measured in 5 mM Tris HCl/NaCl buffer at pH 7.2. Arrow shows a continuous decrease in absorbance of **1** upon increasing DNA concentrations. Inset: Shows a plot of [DNA]/$\Delta\varepsilon_{af}$ vs. [DNA] from Eq. (1). (b) Quenching of fluorescence emission intensities of EthB (12 μM) bound CT-DNA (6.4 μM) at 603 nm (λ_{exc} = 546 nm) in 5 mM Tris HCl/NaCl buffer (pH = 7.2) as a consequence of increasing complex **2** concentrations and arrow shows a decrease in emission intensity upon gradual addition of complex **2** (0–88 μM). Ex and Em slit width = 10 nm. Inset: plot of I/I_0 vs [complex]. (For interpretation of the references to color in this figure, the reader is referred to the web version of this article.)

Table 2
DNA and HSA binding parameters for complexes **1** and **2**.

Complex	K_b[a]/M^{-1}	K_{app}[b]/M^{-1}	K_{HSA} (M^{-1})[c]	k_q(M^{-1} s^{-1})[d]	K (M^{-1})[e]	n[f]
1	(5.87 ± 0.3) × 10^3	1.91 × 10^6	5.63 × 10^5	5.28 × 10^{13}	7.88 × 10^5	1.02
2	(2.10 ± 0.13) × 10^4	1.51 × 10^6	3.00 × 10^5	3.07 × 10^{13}	8.48 × 10^3	0.73

[a] K_b, intrinsic equilibrium DNA binding constant.
[b] K_{app}, apparent DNA binding constant.
[c] K_{HSA}, Stern-Volmer quenching constant for HSA fluorescence.
[d] k_q, Quenching rate constant.
[e] K, binding constant.
[f] n, number of binding sites.

complexes with HSA (1.15 μM) is shown in Figs. 7(a) and S25(a) respectively which demonstrate tryptophan fluorescence emission quenching at 346 nm (λ_{exc} = 295 nm) and hypsochromic shift of ~15 nm with increasing complex concentrations.

The tryptophan emission quenching in HSA results in several molecular interactions that lead to energy transfer, structural or conformational change in protein structure [78]. The static quenching constant (K_{HSA}) for both the complexes were determined using the Stern-Volmer Eq. (4) [79].

The static binding occurs at equilibrium and equilibrium binding constant (K) and the number of site available for protein binding (n) are determined from linear curve–fitting of Scatchard Eq. (6) and represented in Figs. 7(b), S25(b) and Table 2. The calculated K_{HSA} and K values are in the range of 10^5 and 10^3 M^{-1} respectively that suggest moderate binding affinity of the complexes with HSA at a single binding site ($n \sim 1$).

2.5.2. Conformational investigation of HSA binding

Synchronous fluorescence spectra can provide the information related to molecular microenvironment present in the vicinity ofthe multichromophoric entity and the molecule and hence can be used to characterize the various kind of interactions including hydrogen bonds, hydrophobic, van der Waals, etc. between the protein and drug molecule [80]. Scanning the excitation and emission monochromator simultaneously and maintaining a constant interval between them gives the measurement of synchronous fluorescence spectra. The difference of 15 nm and 60 nm between excitation and emission wavelength provide characteristics information about tyrosine and tryptophan moiety respectively in HSA. Upon increasing complex concentration gradually, synchronous fluorescence spectra of HSA (1.15 μM) with Δλ = 15 nm showed a decrease in emission intensity at 285 nm for both complexes, while with Δλ = 60 nm, this decrease observed at 278 nm and 279 nm for complexes **1** and **2** respectively (Figs. 8 and S26). The considerable decrease in intensity with Δλ = 60 nm revealed conformation of HSA changed because of increased hydrophobicity and decreased polarity around tryptophan-214 residue. Similarly, comparatively lower intensity changes with Δλ = 15 nm suggests minor perturbation of environment at the tyrosine residue or this is a secondary effect of binding at trp-214 residue.

2.6. Growth inhibition of Saccharomyces cerevisiae

Despite successful clinical trials and promising results on anticancer activities of ruthenium drugs, their mode of action and various modulating factors are not yet convincing. Here we have used the budding yeast model to understand the biological aspects of tested compounds. Yeast conserves a high degree of similarity with human cells in many cellular and molecular processes and thus a powerful model for studying several molecular mechanisms underlying the pathobiology of several human diseases, including cancer. Recently, we evaluated the molecular insights for mechanism and various chemical, genetic or epigenetic factors for KP1019 activity by using transcriptomics and genetic screening approaches in budding yeast [81]. To investigate the effect of [Ru(im)$_2$(tfa)$_2$] (**1**) and [Ru(in)$_2$(tfa)$_2$] (**2**) on *Saccharomyces cerevisiae* cell growth, we performed yeast serial drop test assay and growth curve assay with wild-type (WT) cells on synthetic complete (SC) agar medium and liquid culture medium respectively. In case of complex **2** treated SC agar plates, cell growth inhibition was observed at a very low dose (20 μM) and the growth was completely inhibited at 30 μM concentration which is promising as compared to that of control plates (Fig. 9(a)) [82]. In case of complex **1** treatment, a considerably higher range of concentration (100 μM–200 μM) was required to observe the inhibitory effects on yeast cell viability (Fig. 9(a)). Similarly, in the liquid medium, both the complexes affected the yeast cell growth in a dose-dependent manner (Fig. 9(b)). These results reveal that the growth rate of yeast cells was reduced upon treatment with complexes

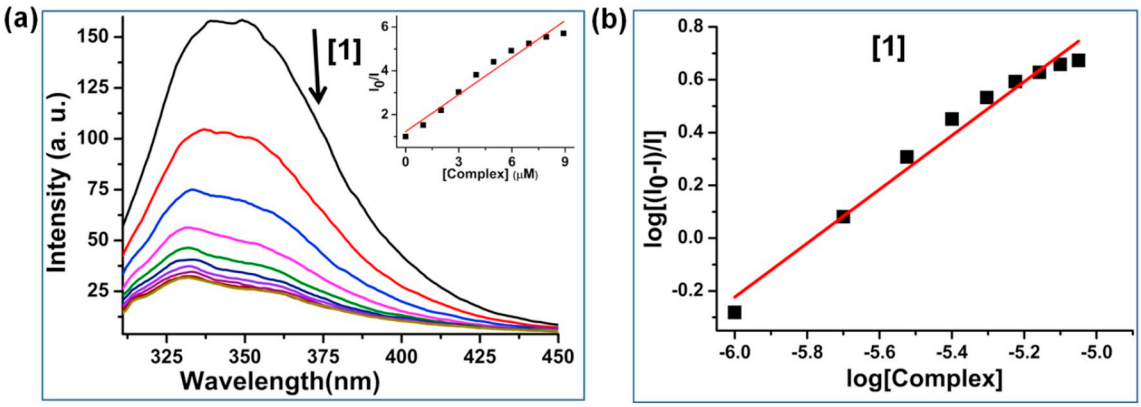

Fig. 7. Binding of complex **1** with HSA: (a) fluorescence emission quenching of HSA (1.15 μM) (in absence and in presence of increasing complex **1** concentration (0–9 μM) in 5 mM Tris-HCl buffer (pH 7.2) at 298 K (λ_{ex} = 295 nm, λ_{em} = 344 nm, slit width = 10/5 nm). Arrow shows a decrease in intensity upon increased [complex]. Inset: Stern-Volmer plot for fluorescence quenching of HSA (b) Scatchard plot: variation of log([I_0-I]/I) as function of log[complex]. (For interpretation of the references to color in this figure, the reader is referred to the web version of this article.)

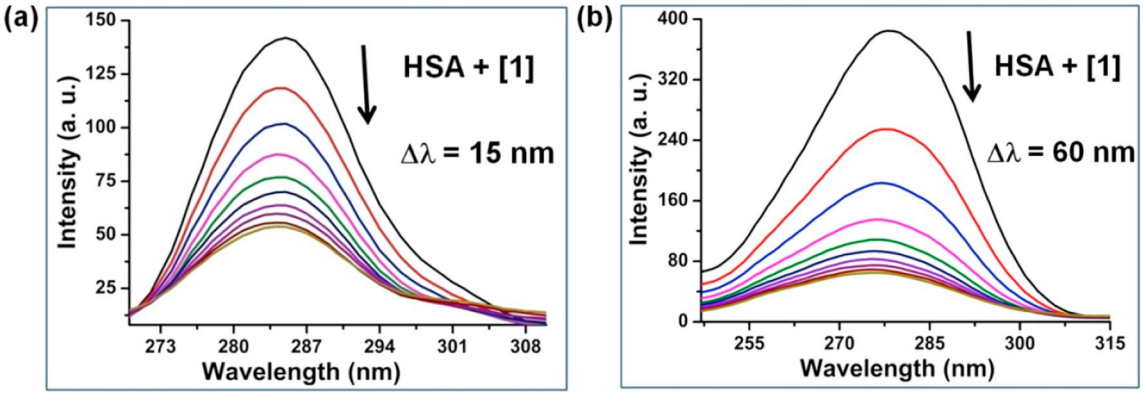

Fig. 8. Synchronous fluorescence spectral measurement of HSA (1.15 μM) in the presence of increased complex **1** concentrations (0–9 μM) with Δλ = 15 nm (a) and Δλ = 60 nm (b) in 5 mM Tris-HCl/5 mM NaCl buffer (pH 7.2) at 298 K. Arrow shows effect of increased complex concentration on HSA fluorescence emission intensity. (For interpretation of the references to color in this figure, the reader is referred to the web version of this article.)

1 and **2**. Besides, complex **2** proves to be more toxic than complex **1** as it shows its inhibitory effects on yeast cell growth at a lower dose as compared to that of the complex **1**. So our results indicate that these two Ru(II) complexes **1** and **2** exhibit toxic effects on yeast cell survivability and show similar kind of activity like ruthenium based anticancer drug KP1019 [81,83,84] (Fig. 9(a)). The presence of more importers or fewer exporters on the plasma membrane and less vacuolar sequestration in case of complex **2** might be potentiating its genotoxic ability by increasing the net availability at the target sites as compared to complex **1** [85–87].

2.7. Cellular uptake and mitochondrial localization studies

The cellular uptake potential and intracellular localization efficacy of the complexes **1** and **2** were evaluated by fluorescence imaging using green filter (EGFP filter, λ_{ex} = 450–490 nm, λ_{em} = 500–550 nm). The microscopy images of yeast cells in response to both the complexes revealed the presence of puncta (2–5) inside the cells, in the cytosol (Fig. 10(a)). As the punctuate structures were present towards the periphery of the cytosol, we hypothesised that the complexes **1** and **2** might be localized to the mitochondria. To ascertain the sub-cellular localization, we performed fluorescence microscopic experiment with WT 4741 strain transformed with plasmid mito-HcRed (HcRed fused to mitochondria targeting sequence) in presence/absence of **1** and **2**. The microscopy images revealed the clear co-localization of the puncta with that of mito-HcRed fluorescence (Fig. 10(b)). To further validate this, we have performed staining experiment with MitoTracker deep red dye that is known to label mitochondria utilizing its negative membrane potential [88]. Cellular images obtained from the above experiment confirmed the sub-cellular localization of both the complexes (**1**, **2**) to mitochondria (Fig. 10(c)). In addition, we ruled out the possibility of these compounds being localized to lipid droplets (LDs) (which also show several punctuate like structures in the cytosol) by performing microscopy experiment using a yeast quadruple mutant (H1246) that is devoid of LDs due to lack of lipid synthesizing enzymes. We treated this mutant with both the compounds and checked for the presence of puncta. The hypothesis was, if the complexes are localizing to the lipid droplets and forming puncta, then we should not observe punctate pattern customary to LDs in case of mutant treated with either of the complexes. But we did observe the puncta in both the WT (Fig. S27(a)) and mutant (Fig. S27(b)), thus ruling out the possibility of the compounds being localized to LDs. Overall these results indicate the effective internalization of the compounds to mitochondria by live yeast cells, despite the presence of its highly rigid cell wall indicating possible efficient internalization in cancer cells.

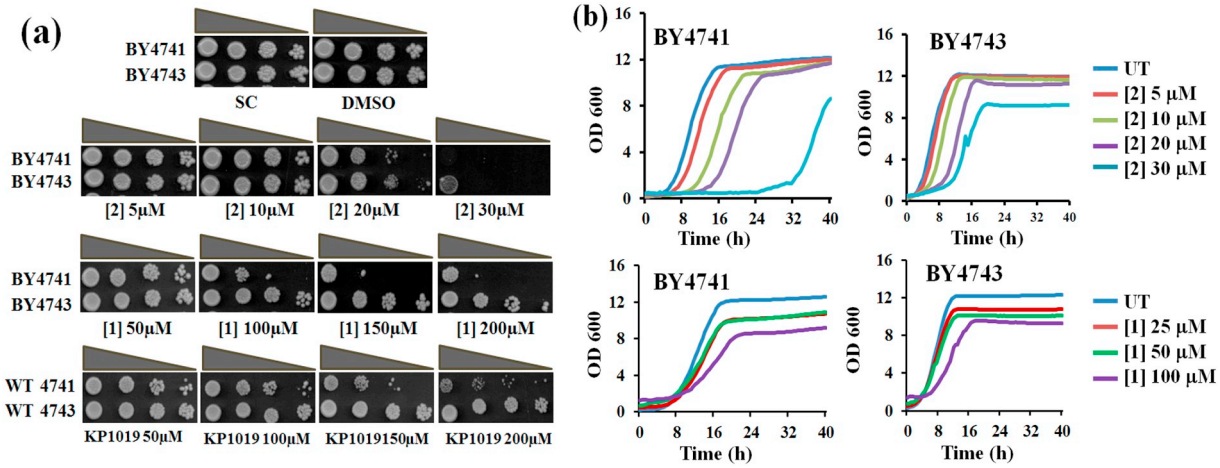

Fig. 9. (a)Yeast serial drop test assay; Wild type (BY4741, BY4743) yeast saturated cultures were ten-fold serially diluted (10^{-1}, 10^{-2}, 10^{-3}, 10^{-4} M) in 1.0 mL of sterile double distilled water and 3 μL of each dilution was spotted on SCA plates containing DMSO (control) or $[Ru(in)_2(tfa)_2]$ (**2**) (5, 10, 20, 30 μM) or $[Ru(im)_2(tfa)_2]$ (**1**) or KP1019 (50, 100, 150, 200 μM). All plates were incubated at 30 °C for 72 h and photographed. (b) Growth curve assay; exponentially growing yeast cultures of the wild-type strain were treated with the indicated concentrations of respective compounds and the growth was monitored by measuring OD_{600} at regular intervals of 30 min for 40 h UT: untreated. (For interpretation of the references to color in this figure, the reader is referred to the web version of this article.)

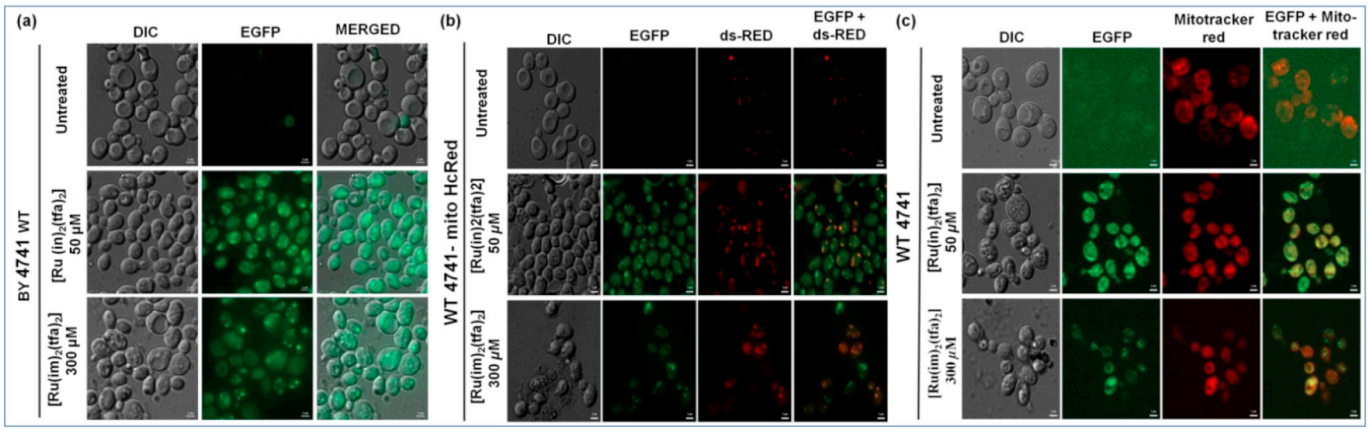

Fig. 10. (a) Fluorescence microscopic visualization and intracellular localization of compounds after treating WT cells for 5 h using EGFP green filter - λ_{ex} = 450–490 nm, λ_{em} = 500–550 nm. DMSO treated cells were taken as control. (b) Pictures of WT cells expressing a mitochondrial red fluorescent marker protein (Mito-hc red) after treatment with **1** and **2** for 5 h using ds-RED filter λ_{ex} = 538–562 nm, λ_{em} = 570–640 nm. (c) Fluorescence microscopic images of WT cells treated with indicated doses of **1** and **2** for 5 h followed by staining with mitotracker red to visualize the mitochondria. Scale bars = 2 μm. Red filter was used with λ_{ex} = 538–562 nm, λ_{em} = 570–640 nm.

2.8. Impairment of mitochondrial function and induction of reactive oxygen species (ROS)

As both the complexes were found to be localized to mitochondria, our next obvious question was to assess the mitochondrial function or respiratory competence of yeast cells in the presence of these complexes. To achieve this, wild type yeast cells were forced to rely on oxidative phosphorylation rather than glycolysis by substituting medium containing glucose (primary fermentable carbon source) with either ethanol or glycerol (non-fermentable carbon source) [89].

Our results (Fig. 11(a)) revealed that the replacement of media glucose with non-fermentable carbon sources increased the susceptibility of yeast cells to the complexes. This growth defect on non-fermentable carbon sources is attributed to impaired mitochondrial oxidative phosphorylation. Moreover, mitochondria are the major sites of ROS production which occurs via electron leakage through oxidative phosphorylation in electron transport chain [90]. Also, higher levels of ROS are produced through excessive electron leakage from impaired mitochondrial oxidative phosphorylation [91]. Therefore, we checked for the accumulation of ROS via staining the compound-treated cells with dihydroethidium (DHE). As shown (Fig. 11(b)), treatment with the compounds triggered a significant increase in the number of DHE positive cells as compared to the control. Above findings suggest the potential role of these Ru(II) complexes as mitochondrial toxicants. These results confirm that the **1** and **2** are likely candidates to introduce the intracellular damage via the formation of ROS. We hypothesize that these Ru(II) active drugs could possibly serve as next-generation anticancer agents.

2.9. Micrococcal nuclease (MNase) assay

To understand whether these compounds alter the global nucleosome occupancy profile or not, we performed Micrococcal nuclease (MNase) assay. However, we could not find any significant alteration in the digestion pattern of treated and untreated samples in response to both the compounds (Fig. 12(a) and (b)). These results suggest that these two complexes are not effective in altering the global chromatin architecture and probably targets specific regions within the genome. $[Ru(im)_2(tfa)_2]$ (**1**) and $[Ru(in)_2(tfa)_2]$ (**2**) hence does not alter the global nucleosome occupancy profile in yeast cells.

3. Conclusions

We strategically designed two Ru(II) complexes comprised of imidazole, indazole and potential NSAID tolfenamic acid to modulate anticancer properties of corresponding KP1019/KP418 drugs. Complexes have been synthesized and characterized using various spectroscopy techniques and structures of complexes have been determined by single crystal X-ray structure determination. Interactions of complexes **1** and **2** with excess of biomolecules L-Arginine, DL-Methionine, GSH, and L(+) ascorbate provide information of ligand substitution and reactivity. The binding of L-arginine and DL-methionine corresponds to arginine deprivation and methionine restriction, respectively as a way of threatening tumor cells. Further, GSH binding may alter cellular GSH level and vitamin-C in combination can suppress the tumor growth. The complexes are moderate binders of DNA and HSA. Complexes exhibit cytotoxicity profile in a dose dependent manner where **1** is comparable with KP1019 and **2** exhibits markedly enhanced growth inhibitory potential than KP1019 in yeast cells. The fluorescence imaging confirmed efficient localization of complexes in mitochondria of yeast cell WT 4741 despite its rigid cell wall and exhibited ROS induced mitochondrial damage. However, the complexes did not show any alteration in nucleosome global occupancy profile in yeast cells. Overall, the designed compounds exhibit high cytotoxicity, mitochondrial targeting, and damaging ability along with sufficient binding ability with several biomolecules. These systems potentially could be explored in terms of COX inhibition, anti-inflammation, and selectivity towards specific cancer cells both in vitro and in vivo as supportive for next-generation anticancer agents.

4. Experimental section

4.1. Materials and methods

$RuCl_3{\cdot}xH_2O$ was purchased from Arora Matthey Pvt. Ltd., India, imidazole, and $AgNO_3$ from Merck (Mumbai, India), indazole from Alfa Aesar, N-(3-Chloro-2 methylphenyl)anthranilic acid from TCI (India) Pvt. Ltd. and solvents were purified before use by following standard procedures [92]. Biochemsitry grade glutathione reduced (GSH), L-arginine, DL-methionine and was purchased from SRL (Mumbai) and L(+) sodium ascorbate from SDFCL (Mumbai). Calf thymus (CT) DNA, human serum albumin (HSA) and ethidium bromide (EthB) were purchased from Sigma Chemicals (USA). Stock buffer solutions were prepared using Milli-Q water (18.2 MΩ). $[(Ru(DMSO)_4Cl_2]$ was prepared following a standard procedure [93]. The presence of C, H, and N were analyzed with Perkin-Elmer 2400 series-II and Perkin-Elmer model 1320 was used to record Fourier transform infrared (FTIR) spectra in KBr pellets within range 4000–400 cm^{-1}. Waters Q-TOF electrospray

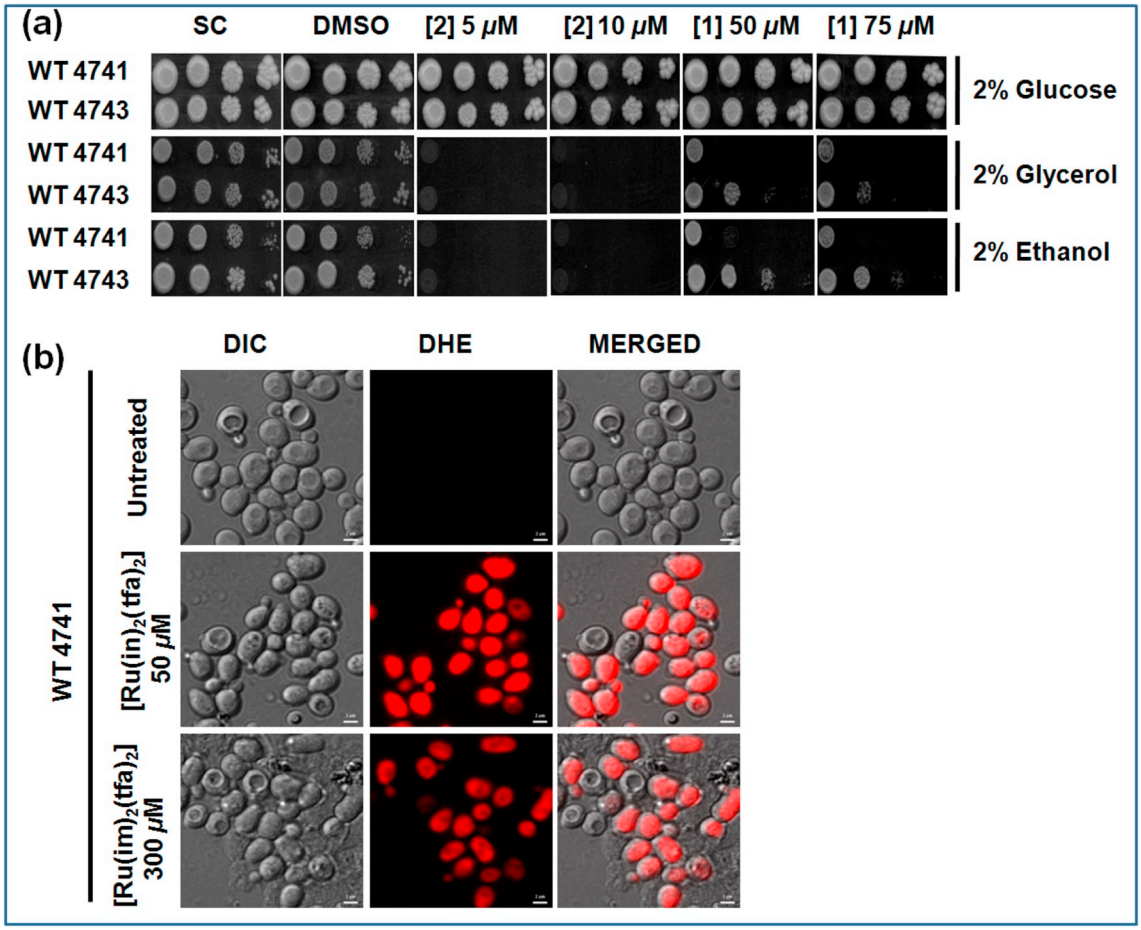

Fig. 11. (a) Growth of wild-type yeast cells in medium containing either 2% glucose or 2% ethanol or 2% glycerol as the carbon source with or without compound treatment. Cells from overnight grown cultures were serially diluted and 3 μL of each dilution spotted onto each plate. Growth was assessed after 5 days incubation at 30 °C. (b) Fluorescence microscopic visualization of wild type yeast cells after giving indicated doses of compound treatment and stained with dihydroethidium (DHE) to visualize ROS producing cells after 3 h of growth. Scale bars = 2 μm. Red filter was used with λ_{ex} = 538–562 nm, λ_{em} = 570–640 nm.

ionization (ESI-MS) spectrometer was used to determine the molecular masses. The ^{1}H NMR spectra were recorded on JEOL instrument with model JNM-ESC400 MHz spectrometer. Chemical shifts values were referenced to the deuterated solvent used. Absorption and fluorescence emission spectra were recorded on Varian V670 and Perkin-Elmer Lambda 25 and Agilent Cary Eclipse spectrophotometer respectively at 298 K. Fluorescence decay were measured using nanosecond time-correlated single photon counting (TCSPC) and steady state fluorescence setup by excitation of samples by laser light of 340 nm. Data was analyzed with DAS6 software of TCSPC instrument and were fitted with multi-exponential function

$$I(t) = \sum a_i \exp - (t/\tau_i)$$

and average lifetime was calculated from following Eq. (1)

$$\bar{\tau} = \frac{\sum_i a_i \tau_i^2}{\sum_i a_i \tau_i} \quad (1)$$

where a_i and τ_i are amplitude and decay time respectively of ith component of multi-exponential decay curve [94].

Cyclic voltametric measurements were carried out in DMF using CH Instrument Model CHI 610E potentiostat and TBAP (0.1 M) as supporting electrolyte containing 1 mM complex concentration. Platinum, Ag/AgCl and glassy carbon was used as auxiliary, reference, and working electrode respectively.

4.2. Strains, chemicals, growth media, and growth conditions

The *Saccharomyces cerevisiae* strains used in this study are WT-BY4741 (MATa his3Δ1 leu2Δ0 met15Δ0 ura3Δ0; Axel Mogk [95]), WT-BY4743 (MATa/α his3Δ1/his3Δ1 leu2Δ0/leu2Δ0 LYS2/lys2Δ0 met15Δ0/MET15 ura3Δ0/ura3Δ0; Yeast Knockout Collection-Open Biosystems), WT SCY62 (MATa his3-11,15 leu2-3, 112 ura3-1 trp1-1 can1-100 ADE2; StenStymne [96]) and mutant H1246 (MATα are1Δ::HIS3 are2Δ::LEU2 dga1Δ::KanMX4 lro1Δ::TRP1 ADE2; are1Δare2Δdga1Δlro1Δ; StenStymne [96]). All yeast strains used in this study were grown in synthetic complete (SC) liquid media containing 2% glucose at 30 °C. SC liquid media was prepared by mixing all the components like-amino acids, yeast nitrogen base (YNB) and ammonium sulphate (AS) by following a standard protocol (Yeast Protocols Handbook, Clontech laboratories, Inc.). The wild-type BY4741 strain was transformed with a plasmid MitoHcRed (URA3) (gifted by Dr. Rong Li Lab) using the standard lithium acetate procedure [97] and the resultant transformants were propagated in Uracil drop-out liquid media. For solid agar media, 2% Bacto-agar was used in addition to SC media components. Media components and all other reagents used in this study were of molecular biology grade, purchased from Sigma–Aldrich, Merck, Himedia, GE Healthcare, Invitrogen, New England BioLabs and Thermo Fisher Scientific.

4.3. Synthesis of [Ru(im)$_2$(tfa)$_2$] (1) and [Ru(in)$_2$(tfa)$_2$] (2)

The complexes **1** and **2** were synthesized by adding ethanolic

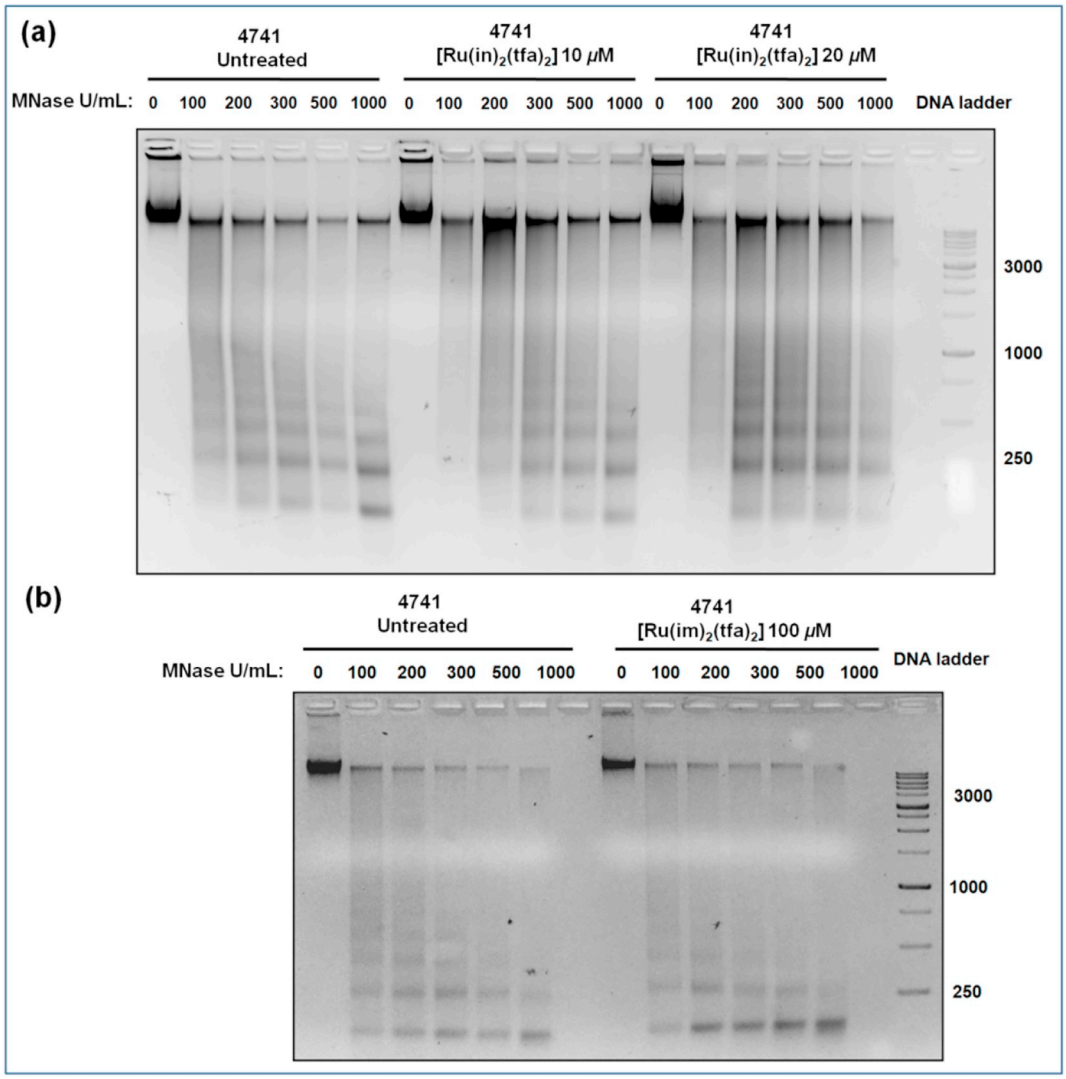

Fig. 12. The wild type yeast cells were treated with DMSO or $[Ru(in)_2(tfa)_2]$ (**2**) (10 μM, 20 μM) (a) and $[Ru(im)_2(tfa)_2]$ (**1**) (100 μM) (b) for 3 h at 30 °C and equal numbers of cells were processed for MNase digestion. MNase was used with increasing concentration (0, 100, 200, 300, 500 and 1000 U/mL). Samples were run on 1.5% agarose gel, together with DNA ladder, and stained with ethidium bromide.

solutions (3 mL) of imidazole (im) (31 mg, 0.4554 mmol for **1**) and indazole (in) (54 mg, 0.4571 mmol for **2**) to a boiling solution of $[(Ru(DMSO)_4Cl_2]$ (100 mg, 0.2064 mmol) in ethanol (15 mL) to obtain a clear yellowish and greenish solution respectively. The reaction was stirred under reflux for 6 h, followed by addition of $AgNO_3$ (77 mg, 0.4532 mmol) and stirring was continued at RT for next 3 h. The colorless AgCl precipitate was filtered off through a sintered glass crucible (G-4) and neutralized tolfenamic acid (119 mg, 0.4547 mmol) with KOH (26 mg, 0.4635 mmol) in ethanol (2 mL) was added and refluxed overnight. The resulting dark green (**1**) and brown (**2**) solution obtained was evaporated to yield microcrystalline solids. The solids were washed thoroughly with DCM (**1**), and cold water followed by Et_2O (**2**) and dried in vacuum over silica. Crystals of **1** was obtained from ethanolic solution layered with benzene while complex **2** was crystallized as **2**·2$CHCl_3$ by vapour diffusion of pentane to a chloroform solution of complex.

4.3.1. *[Ru(im)$_2$(tfa)$_2$] (1)*

Yield:110 mg (70%). Anal. calcd for $C_{34}H_{30}Cl_2N_6O_4Ru$: C, 53.83; H, 3.99; N, 11.08. Found: C, 53.72; H, 3.89; N, 10.98. ESI-MS (DMF): *m/z* 757.07 $[M-H]^+$ (calc. for $C_{34}H_{29}N_6O_4Cl_2Ru$: *m/z* 757.07). FT-IR (KBr, ν/cm^{-1}): 3432 (w), 3238 (w), 2930 (w), 2396 (w), 1763 (w), 1609 (s, sh), 1579 (vs, sh,$\nu_{as}COO^-$), 1555 (s, sh), 1494 (vs, sh), 1460 (s) 1377 (vs, ν_s COO^-), 1287 (s, sh), 1149 (m), 1074 (w), 1041 (w), 1014 (m), 906 (w), 882 (w), 865 (w), 825 (w), 785 (w), 755 (s, sh), 705 (w), 667 (w), 602 (w), 523 (w) [vs, very strong; s, strong; m, medium, w, weak; br, broad; sh; sharp]. ^1H NMR (400 MHz, DMSO-d_6) δ 11.93 (s, 2H), 7.93 (d, 2H), 7.29 (d, 3H), 7.16–7.08 (m, 6H), 7.02 (d, 3H), 6.96 (d, 3H), 6.69–6.65 (m, 3H), 2.29 (s, 6H). UV–visible in DMF [λ_{max}, nm (ε, M^{-1} cm^{-1})]: 300 (23770), 480 (2970) and 738 (4690).

4.3.2. *[Ru(in)$_2$(tfa)$_2$] (2)*

Yield:121 mg (68%). Anal. calcd for $C_{42}H_{34}Cl_2N_6O_4Ru$: C, 58.74; H, 3.99; N, 9.79. Found: C, 58.72; H, 3.94; N, 9.76. ESI-MS (DMF): *m/z* 859.10 $[M + H]^+$ (calc. for $C_{42}H_{35}N_6O_4Cl_2Ru$: *m/z* 859.11). FT-IR (KBr, ν/cm^{-1}): 3425 (m), 3064 (w), 2923 (w), 1922 (w), 1609 (s, sh), 1581 (vs, sh, $\nu_{as}COO^-$), 1499 (s, sh), 1456 (s, sh), 1372 (s, sh,$\nu_s COO^-$), 1355 (s), 1284 (m), 1240 (w), 1208 (w), 1172 (w), 1147 (w), 1012 (s), 952 (w), 908 (w), 881 (w), 837 (w), 741 (s, sh), 703 (m), 670 (w), 433 (w). ^1H NMR (400 MHz, DMSO-d_6) δ 13.03 (s, 2H), 9.78 (s, 2H), 8.06 (s, 1H), 7.91 (d, 2H), 7.75 (d, 2H), 7.53 (d, 2H), 7.37–7.28 (m, 6H), 7.22 (d, 4H), 7.13–7.07 (m, 3H), 6.84 (d, 2H), 6.79–6.74 (m, 2H), 2.26 (s, 6H). UV–visible in DMF [λ_{max}, nm (ε, M^{-1} cm^{-1})]: 290 (28410), 509 (1660), 741 (1225).

4.4. Solubility and stability

The complexes **1** and **2** were soluble in DMF and DMSO and were sparingly soluble in water, acetonitrile and insoluble in EtOAc, Et_2O, THF, and hydrocarbons. The complex **2** was also soluble in DCM and $CHCl_3$. The solution-state stability of complexes was determined by time-dependent ^{1}H NMR, UV–vis absorption and from ESI-MS spectral analyses.

4.5. Single crystal X-ray structure determinations

Crystals of suitable dimensions for complexes **1** and **2**·$CHCl_3$ were grown at room temperature (298 K) and mounted over glass fiber. Diffraction data were collected at 100(2) K with a Bruker D8 Quest Microfocus X-ray CCD diffractometer attached to an Oxford Cryo systems device. X-ray beam obtained from Mo Kα radiation (λ = 0.71073 Å) possessing ω-scanner (width of 0.5° per frame) operated with manufacturer's APEX2 v2012.4-3 software package at a scan speed of 5 s/frame [98]. Intensity data collected in ω-2θ scan mode were corrected for Lorentz-polarization effects, processed and integrated with Bruker's SAINT software [99]. SADABS programme [100] used for multiscan absorption corrections; XPREP for space group determination and structure was solved using SHELXS-97 [101]. Structure refinement processed using WinGX 1.70 inbuilt SHELXL-97 [102] using full matrix least square technique with SHELXTL 6.14 software package [103]. Non-hydrogen atoms were refined anisotropically and all hydrogen atoms were included in their calculated position and refined using a riding model. Structural representations were generated using ORTEP [104]. Crystallographic data and refinement parameter are listed in Table S1, selected bond distances and angles are given in Table S2 in SI. The CCDC deposition number for complexes **1** and **2** are 1872898 and 1872899 respectively.

4.6. Interactions with L-arginine, DL-methionine, L(+) ascorbate

A stock solution of these bioactive ligands was prepared in 5 mM Tris-HCl/NaCl (pH 7.2) buffer and emission spectral traces were recorded after addition to complexes **1** and **2** under similar conditions at 298 K in DMF.

4.7. Binding interaction with DNA

4.7.1. UV–visible spectral experiments

A fresh solution of CT-DNA in 5 mM tris-HCl/NaCl, pH 7.2 buffer were prepared and stored at 4 °C. The purity of CT-DNA from RNA and protein was confirmed by its absorbance ratio value at A_{260}/A_{280} as 1.9:1 [105]. Concentration of DNA (stock = 220 μM) was obtained from ε_{260} = 6600 M^{-1} cm^{-1} and respective absorbance values (A_{260}) [106]. The solution of metal complex in DMF was prepared and absorption spectra were measured by a gradual increase of CT-DNA concentration to the fixed concentrations of metal complexes solution. Intrinsic equilibrium DNA binding constant (K_b) value for complexes was determined by following half-reciprocal Eq. (2)

$$[DNA]/(\varepsilon_a - \varepsilon_f) = [DNA]/(\varepsilon_b - \varepsilon_f) + 1/K_b(\varepsilon_b - \varepsilon_f) \quad (2)$$

where [DNA] signifies the concentration of DNA, ε_a the apparent molar extinction coefficient, ε_f, and ε_b are molar extinction in free from DNA and in fully bound state, respectively [107]. DNA binding constant were calculated from slope to intercept ratio of linear fit of [DNA] / ($\varepsilon_a - \varepsilon_f$) vs. [DNA] plots.

4.7.2. Competitive binding by emission spectral experiments

Ethidium bromide displacement assay was performed for complexes in 5 mM tris-HCl/NaCl, pH 7.2 by monitoring fluorescence emission traces of ethidium bromide bound DNA at 603 nm (λ_{ex} = 546 nm) by gradual increase of metal complex concentrations at 298 K. Addition of complexes was continued till 50% decrease in emission intensity and apparent binding constants (K_{app}) obtained by Eq. (3)

$$K_{app} \times C_{50} = K_{EthB} \times [EthB] \quad (3)$$

where, $K_{EthB} = 1 \times 10^7\ M^{-1}$ is binding constant for ethidium with DNA, [EthB] = concentration of ethidium bromide, C_{50} = complex concentration at 50% decrease of emission intensity [108].

4.8. Protein binding experiments

4.8.1. Human serum albumin binding emission experiments

Binding of complexes to human serum albumin (HSA) protein was determined in 5 mM tris HCl-NaCl, pH 7.2 buffer by tryptophan fluorescence emission quenching measurement. Initially, 1 μM solution of HSA in buffer medium was excited with 295 nm and resulting emission spectra were measured. Consequently, complex solution in DMF was added to it and quenching of emission were recorded at 345 nm and quenching constant was obtained from the slope of the linear fit of Stern-Volmer Eq. (4) [109].

$$I_0/I = 1 + K_{HSA}[Q] \quad (4)$$

$$I_0/I = 1 + k_q \tau_0 [Q] \quad (5)$$

where symbols I_0 and I are tryptophan emission intensities in absence and in presence of quencher (Complex). The terms k_q represents quenching rate constant and τ_0 the average lifetime (~10^{-8} s) of HSA without quencher. Assuming the binding of complexes to HSA at equilibrium, the number of the binding sites available and equilibrium binding constant was calculated from Scatchard Eq. (6) [110]

$$\log(I_0 - I)/I = \log K + n \log[Q] \quad (6)$$

where K is the binding constant of compounds at equilibrium and n is the number of binding sites. A linear fit of log (I_0-I)/I vs. log[Q] gives n as slope and K as intercept.

4.8.2. Synchronous fluorescence emission experiments

Synchronous fluorescence spectra with two different Δλ (the difference between λ_{exc} and λ_{em} of HSA) 15 nm and 60 nm in the range from 225 nm to 400 nm were recorded simultaneously in an identical experimental condition of instrument sensitivity used for HSA binding measurements [111].

4.9. Cell growth sensitivity and growth curve assays

Growth sensitivity assay was performed to examine the biological effect of $[Ru(im)_2(tfa)_2]$ (**1**) and $[Ru(in)_2(tfa)_2]$ (**2**) on the growth of yeast cells as described previously [112]. In brief, overnight grown cultures of wild-type (WT) BY4741 and BY4743 yeast cells were tenfold serially diluted (10^{-1}, 10^{-2}, 10^{-3}, 10^{-4} M) and 3 μL of each was spotted onto solid SC (synthetic complete)-agar plates without (DMSO control) or with the addition of respective compounds at indicated doses. All the plates were incubated at 30 °C and growth of yeast strains was recorded after 72 h by scanning the plates using a HP scanner.

For growth curve analysis, exponentially growing yeast cells were treated with either DMSO (control) or indicated doses of either $[Ru(im)_2(tfa)_2]$ (**1**) and $[Ru(in)_2(tfa)_2]$ (**2**) in duplicate manner and then seeded onto a 96-well cell culture plate (SPL Life Sciences Ltd.). Growth curves were analyzed for each treatment using representative optical density (OD_{600}) values measured at a regular interval of 30 min for a time-period of 40 h using an automatic plate reader (Eon™ Microplate Spectrophotometer).

4.10. Fluorescence imaging

To investigate the uptake of these emissive compounds in wild type yeast cells (BY 4741), we performed fluorescence imaging experiment.

For this, the exponentially growing wild type cells were either left untreated (DMSO control) or treated with $[Ru(im)_2(tfa)_2]$ (**1**) and $[Ru(in)_2(tfa)_2]$ (**2**) for 5 h at 30 °C. The cells were then washed with 1X PBS buffer (pH-7.4) three times and imaged using 100× oil-immersion objective lens of ZEISS ApoTome.2 microscope equipped with the appropriate filter (EGFP filter, λ_{ex} = 450–490 nm, λ_{em} = 500–550 nm). Further, all the images were processed using ZEN-2012 (Blue edition) software. In case of staining the cells with MitoTracker Deep Red (Invitrogen), prior to washing, cells were incubated with this molecular probe for 3–5 min. For dihydroethidium (DHE) staining, treated cells were incubated with DHE for 1 h in rotamer followed by washing with PBS and visualization.

4.11. Micrococcal nuclease (MNase) assay

To investigate the effect of the compounds on global nucleosome occupancy profile, we performed MNase assay as described previously [113] with slight modifications. Briefly, exponentially growing yeast cells were treated with DMSO (control) or $[Ru(in)_2(tfa)_2]$ (**2**) (10 μM, 20 μM) and $[Ru(im)_2(tfa)_2]$ (**1**) (100 μM) for 3 h at 30 °C. Equal number of cells were then processed for MNase digestion. At first, spheroplasts were made from ~100 OD cells by lyticase (SIGMA) digestion and then processed further for digestion with MNase as per dilution series to make 0, 100, 200, 300, 500 and 1000 U/mL concentrations (dilution buffer-50 mM Tris pH 7.9, 5 mM $CaCl_2$). MNase (New England Biolabs-NEB, M0247S) digestion was performed for 3 min at 37 °C, and the reaction was stopped immediately by adding stop solution (0.25 M EDTA, 5% SDS). The samples were then subjected to overnight Proteinase K digestion at 37 °C. Following day, phenol-chloroform extraction was carried out to isolate DNA; pellets were washed with 70% ethanol, air-dried, and re-suspended in 30 μL of 1X TE containing 100 mg/mL RNase. Samples were loaded on a 1.5% agarose gel and visualized by EthB staining.

Abbreviations

im	1*H*-imidazole
in	1*H*-indazole
tfa	Tolfenamic acid
ESI-MS	Electrospray ionization mass spectroscopy
FT-IR	Fourier Transformed Infrared spectroscopy
NSAID	Nonsteroidal anti-inflammatory drug
Tris	Tris(hydroxymethyl) aminomethane
GSH	Glutathione
CT	Calf thymus
EthB	Ethidium bromide
HSA	Human serum albumin
MNase	Micrococcal nuclease
ROS	Reactive oxygen species

Acknowledgements

We thank the Science and Engineering Research Board (SERB), India for financial support (Project no. EMR/2016/000521). The CSIR is acknowledged for supporting (File No. 38(1468)/18/EMR-II) this work financially to RST. P. K. thanks University Grants Commission (U.G.C.), SS thanks CSIR, S. D. thanks Ministry of Human Resource Development (MHRD) for their respective research fellowships. Dr. Rong Li is acknowledged for gifting us mito-HcRed plasmid.

Appendix A. Supplementary data

Supplementary data to this article can be found online at https://doi.org/10.1016/j.jinorgbio.2019.110769.

References

[1] American Cancer Society, Cancer Facts and Figures, (2017).
[2] L. Kelland, Nat. Rev. 7 (2007) 573–584.
[3] T.C. Johnstone, K. Suntharalingam, S.J. Lippard, Chem. Rev. 116 (2016) 3436–3486.
[4] T.C. Johnstone, J.J. Wilson, S.J. Lippard, Inorg. Chem. 52 (2013) 12234–12249.
[5] A.V. Klein, T.W. Hambley, Chem. Rev. 109 (2009) 4911–4920.
[6] G. Sava, K. Clerici, I. Capozzi, M. Cocchietto, R. Gagliardi, E. Alessio, G. Mestroni, A. Perbellini, Anti-Cancer Drugs 10 (1999) 129–138.
[7] P.J. Dyson, G. Sava, Dalton Trans. (2006) 1929–1933.
[8] A. Bergamo, G. Sava, Dalton Trans. 40 (2011) 7817–7823.
[9] A. Bergamo, G. Sava, Chem. Soc. Rev. 44 (2015) 8818–8835.
[10] K.-G. Lipponer, E. Vogel, B.K. Keppler, Met.-Based Drugs 5 (1996) 243–260.
[11] C.G. Hartinger, S. Zorbas-Seifried, M.A. Jakupec, B. Kynast, H. Zorbas, B.K. Keppler, J. Inorg. Biochem. 100 (2006) 891–904.
[12] R. Trondl, P. Heffeter, C.R. Kowol, M.A. Jakupec, W. Berger, B.K. Keppler, Chem. Sci. 5 (2014) 2925–2932.
[13] S. Thota, D.A. Rodrigues, D.C. Crans, E.J. Barreiro, J. Med. Chem. 61 (2018) 5805–5821.
[14] E. Alessio, Eur. J. Inorg. Chem. 2017 (2017) 1549–1560.
[15] R.G. Kenny, C.J. Marmion, Chem. Rev. 119 (2019) 1058–1137.
[16] A.K. Bytzek, K. Boeck, G. Hermann, S. Hann, B.K. Keppler, C.G. Hartinger, G. Koellensperger, Metallomics 3 (2011) 1049–1055.
[17] G. Sava, S. Zorzet, C. Turrin, F. Vita, M.R. Soranzo, G. Zabucchi, M. Cocchietto, A. Bergamo, S. DiGiovone, G. Pezzoni, L. Sartor, S. Garbisa, Clin. Cancer Res. 9 (2003) 1898–1905.
[18] S. Leijen, S.A. Burgers, P. Baas, D. Pluim, M. Tibben, E. van Werkhoven, E. Alessio, G. Sava, J.H. Beijnen, J.H. Schellens, Investig. New Drugs 33 (2015) 201–214.
[19] I. Khalaila, A. Bergamo, F. Bussy, G. Sava, P.J. Dyson, Int. J. Oncol. 29 (2006) 261–268.
[20] A. Bergamo, C. Gaiddon, J.H.M. Schellens, J.H. Beijnen, G. Sava, J. Inorg. Biochem. 106 (2012) 90–99.
[21] B.K. Keppler, W. Rupp, J. Cancer Res. Clin. Oncol. 111 (1986) 166–168.
[22] C.G. Hartinger, M.A. Jakupec, S. Zorbas-Seifried, M. Groessl, A. Egger, W. Berger, H. Zorbas, P.J. Dyson, B.K. Keppler, KP1019, Chem. Biodivers. 5 (2008) 2140–2155.
[23] E.S. Antonarakis, A. Emadi, Cancer Chemother. Pharmacol. 66 (2010) 1–9.
[24] H. Chen, J.A. Parkinson, S. Parsons, R.A. Coxall, R.O. Gould, P.J. Sadler, J. Am. Chem. Soc. 124 (2002) 3064–3082.
[25] H. Chen, J.A. Parkinson, R.E. Morris, P.J. Sadler, J. Am. Chem. Soc. 125 (2003) 173–186.
[26] H.-K. Liu, S.J. Berners-Price, F. Wang, J.A. Parkinson, J. Xu, J. Bella, P.J. Sadler, Angew. Chem. Int. Ed. 45 (2006) 8153–8156.
[27] A. Bergamo, A. Masi, A.F.A. Peacock, A. Habtemariam, P.J. Sadler, G. Sava, J. Inorg. Biochem. 104 (2010) 79–86.
[28] X. Meng, M.L. Levya, J.M. Gross, S. Benosman, B. Fricker, S. Harlepp, P. Hebraud, A. Boos, P. Wlosik, P. Bischoff, C. Sirlin, M. Pfeffer, J.P. Loeffler, C. Gaiddon, Cancer Res. 69 (2009) 5458–5466.
[29] C.S. Allardyce, P.J. Dyson, D.J. Ellis, S.L. Heath, Chem. Commun. (2001) 1396–1397.
[30] C. Scolaro, A. Bergamo, L. Brescacin, R. Delfino, M. Cocchietto, G. Laurenczy, T.J. Geldbach, G. Sava, P.J. Dyson, J. Med. Chem. 48 (2005) 4161–4171.
[31] E. Estebanez-Perpina, L.A. Arnold, P. Nguyen, E.D. Rodrigues, E. Mar, R. Bateman, P. Pallai, K.M. Shokat, J.D. Baxter, R.K. Guy, P. Webb, R.J. Fletterick, Proc. Natl. Acad. Sci. U. S. A. 104 (2007) 16074–16079.
[32] J.L. Liggett, X. Zhang, T.E. Eling, S.J. Baek, Cancer Lett. 346 (2014) 217–224.
[33] A. Eskandari, J.N. Boodram, P.B. Cressey, C. Lu, P.M. Bruno, M.T. Hemann, K. Suntharalingam, Dalton Trans. 45 (2016) 17867–17873.
[34] U. Basu, B. Banik, R. Wen, R.K. Pathak, S. Dhar, Dalton Trans. 45 (2016) 12992–13004.
[35] L. Hiľovská, R. Jendželovský, P. Fedoročko, Mol. Clin. Oncol. 3 (2015) 3–12.
[36] M. Zampakou, N. Rizeq, V. Tangoulis, A.N. Papadopoulos, F. Perdih, I. Turel, G. Psomas, Inorg. Chem. 53 (2014) 2040–2052.
[37] J.N. Boodram, I.J. McGregor, P.M. Bruno, P.B. Cressey, M.T. Hamann, K. Suntharalingam, Angew. Chem. Int. Ed. 55 (2016) 2845–2850.
[38] K. Kim, J. Yoon, J. Kim, S.J. Baek, T.E. Eling, W. Lee, J. Ryu, J. Lee, J. Lee, J. Yoo, Biochem. Biophys. Res. Commun. 325 (2004) 1298–1303.
[39] S.J. Baek, K.S. Kim, J.B. Nixon, L.C. Wilson, T.E. Eling, Mol. Pharmacol. 59 (2001) 901–908.
[40] Y. Tatematsu, H. Hayashi, R. Taguchi, H. Fujita, A. Yamamoto, K. Ohkura, Biol. Pharm. Bull. 39 (2016) 278–284.
[41] A.H. Kachroo, J.M. Laurent, C.M. Yellman, A.G. Meyer, C.O. Wilke, E.M. Marcotte, Science 348 (2015) 921–925.
[42] V. Khurana, S. Lindquist, Nat. Rev. Neurosci. 11 (2010) 436–449.
[43] R. Matuo, F.G. Sousa, D.G. Soares, D. Bonatto, J. Saffi, A.E. Escargueil, A.K. Larsen, J.A. Henriques, Cancer Chemother. Pharmacol. 70 (2012) 491–502.
[44] P.K. Sahu, R.S. Tomar, J. Biol. Chem 294 (2019) 3837–3852.
[45] M. Leao, C. Pereira, A. Bisio, Y. Ciribilli, A.M. Paiva, N. Machado, A. Palmeira, M.X. Fernandes, E. Sousa, M. Pinto, A. Inga, L. Saraiva, Biochem. Pharmacol. 85 (2013) 1234–1245.
[46] S. Tsiliou, L.-A. Kefala, F. Perdih, I. Turel, D.P. Kessissoglou, G. Psomas, Eur. J. Med. Chem. 48 (2012) 132–142.
[47] E.L. Hawksworth, P.C. Andrews, W. Lie, B. Lai, C.T. Dillon, J. Inorg. Biochem. 135 (2014) 28–39.

[48] M.A. Jakupec, E. Reisner, A. Eichinger, M. Pongratz, V.B. Arion, M. Galanski, C.G. Hartinger, B.K. Keppler, J. Med. Chem. 48 (2005) 2831–2837.
[49] G.E. Büchel, I.N. Stepanenko, M. Hejl, M.A. Jakupec, B.K. Keppler, V.B. Arion, Inorg. Chem. 50 (2011) 7690–7697.
[50] S. Ahmed, N. Mustaan, M.A. Sheraz, S.A.A. un Nabi, I. Ahmad, Int. J. Pharm. 2015 (2015) 1–8.
[51] J. Gu, Y. Yan, B.J. Helbig, Z. Huang, T. Lian, R.H. Schmehl, Coord. Chem. Rev. 282–283 (2015) 100–109.
[52] E. Amouyal, M. Mouallem–Bahout, J. Chem. Soc. Dalton Trans. (1992) 509–513.
[53] E. Reisner, V.B. Arion, A. Rufińska, I. Chiorescu, W.F. Schmid, B.K. Keppler, Dalton Trans. (2005) 2355–2364.
[54] M.J. Rose, N.L. Fry, R. Marlow, L. Hinck, P.K. Mascharak, J. Am. Chem. Soc. 130 (2008) 8834–8846.
[55] A. Mandal, M.A. Hoque, A. Grupp, A. Paretzki, W. Kaim, G.K. Lahiri, Inorg. Chem. 55 (2016) 2146–2156.
[56] C.A. Vock, C. Scolaro, A.D. Phillips, R. Scopelleti, G. Sava, P.J. Dyson, J. Med. Chem. 49 (2006) 5552–5561.
[57] F. Manig, K. Kuhne, C. von Neubeck, U. Schwarzenbolz, Z. Yu, B.M. Kessler, J. Pietzsch, L.A. Kunz-Schughart, J. Biotechnol. 242 (2017) 30–54.
[58] R.C. Geck, A. Toker, Adv. Biol. Regul. 62 (2016) 11–17.
[59] F. Qiu, J. Huang, M. Sui, Cancer Lett. 364 (2015) 1–7.
[60] C.-C. Huang, S.-T. Tsai, C.-C. Kuo, J.S. Chang, Y.-T. Jin, J.-Y. Chang, J.-R. Hsiao, Oral Oncol. 48 (2012) 1227–1235.
[61] Y. Bobak, Y. Kurlishchuk, B. Vynnytska-Myronovska, O. Grydzuk, G. Shuvayeva, M.J. Redowicz, L.A. Kunz-Schughart, O. Stasyk, Int. J. Biochem. Cell Biol. 70 (2016) 29–38.
[62] E. Cellarier, X. Durando, M.P. Vasson, M.C. Farges, A. Demiden, J.C. Maurizis, J.C. Madelmont, P. Chollet, Cancer Treat. Rev. 29 (2003) 489–499.
[63] P. Cavuoto, M.F. Fenech, Cancer Treat. Rev. 38 (2012) 726–736.
[64] J.H. Wu, G. Batist, Biochim. Biophys. Acta 1830 (2013) 3350–3353.
[65] W.H. Ang, I. Khalaila, C.S. Allardyce, L. Juillerat-Jeanneret, P.J. Dyson, J. Am. Chem. Soc. 127 (2005) 1382–1383.
[66] C.-H. Wang, H.T. Wu, H.M. Cheng, T.-J. Yen, I.-H. Lu, H.C. Chang, S.-C. Jao, T.K.M. Shing, W.-S. Li, J. Med. Chem. 54 (2011) 8574–8581.
[67] E.-Y. Gong, Y.J. Shin, I.-Y. Hwang, J.H. Kim, S.-M. Kim, J.-H. Moon, J.-S. Shin, D.-H. Lee, D.Y. Hur, D.-H. Jin, S.-W. Hong, W.K. Lee, W.-J. Lee, Toxicol. Lett. 258 (2016) 126–133.
[68] C.M. Kurbacher, U. Wagnera, B. Kolster, P.E. Andreotti, D. Krebs, H.W. Bruckner, Cancer Lett. 103 (1996) 183–189.
[69] P.M. Takahara, C.A. Frederick, S.J. Lippard, J. Am. Chem. Soc. 118 (1996) 12309–12321.
[70] J.C. Genereux, J.K. Barton, Chem. Rev. 110 (2010) 1642–1662.
[71] M.R. Gill, J.A. Thomas, Chem. Soc. Rev. 41 (2012) 3179–3192.
[72] J.M. Kelly, A.B. Tossi, D.J. McConnell, C. OhUigin, Nucleic Acids Res. 13 (1985) 6017–6034.
[73] M.J. Waring, J. Mol. Biol. 13 (1965) 269–282.
[74] F.J. Meyer-Almes, D. Porschke, Biochemistry 32 (1993) 4246–4253.
[75] F.D. Abreu, T.F. Paulo, M.H. Gehlen, R.A. Ando, L.G.F. Lopes, A.C.S. Gondim, M.A. Vasconcelos, E.H. Teixeria, E.H.S. Sousa, I.M.M. de Carvalho, Inorg. Chem. 56 (2017) 9084–9096.
[76] X.M. He, D.C. Carter, Nature 358 (1992) 209–215.
[77] A. Sulkowska, J. Mol. Struct. 614 (2002) 227–232.
[78] N.S. Quiming, R.B. Vergel, M.G. Nicolas, J.A. Villanueva, J. Health Sci. 51 (2005) 8–15.
[79] Y. Wang, H. Zhang, G. Zhang, W. Tao, S. Tang, J. Lumin. 126 (2007) 211–218.
[80] Y.J. Hu, Y. Liu, X.H. Xiao, Biomacromolecules 10 (2009) 517–521.
[81] U. Golla, S. Swagatika, S. Chauhan, R.S. Tomar, Oncotarget 8 (2017) 98426–98454.
[82] S. Ishida, J. Lee, D.J. Thiele, I. Herskowitz, Proc. Natl. Acad. Sci. U. S. A. 99 (2002) 14298–14302.
[83] V. Singh, G.K. Azad, P. Mandal, M.A. Reddy, R.S. Tomar, FEBS Lett. 588 (2014) 1044–1052.
[84] V. Singh, G.K. Azad, M.A. Reddy, S. Baranwal, R.S. Tomar, Eur. J. Pharmacol. 736 (2014) 77–85.
[85] D.J. Katzmann, T.C. Hallstrom, M. Voet, W. Wysock, J. Golin, G. Volckaert, W.S. Moye-Rowley, Mol. Cell. Biol. 15 (1995) 6875–6883.
[86] R.J.D. Reid, E.A. Kauh, M.A. Bjornsti, J. Biol. Chem. 272 (1997) 12091–12099.
[87] L.A. Hazelwood, M.C. Walsh, J.T. Pronk, J.M. Daran, Appl. Environ. Microbiol. 76 (2010) 318–328.
[88] B. Chazotte, Cold Spring Harb Protoc 2011 (2011) 990–992.
[89] M.G. Baile, S.M. Claypool, Front Biosci (Landmark Ed) 18 (2013) 241–278.
[90] M.P. Murphy, Biochem. J. 417 (2009) 1–13.
[91] C. Guo, L. Sun, X. Chen, D. Zhang, Neural Regen. Res. 8 (2013) 2003–2014.
[92] W. L. F. Armarego, D. D. Perrin, Butterworth Heinemann, Oxford, Boston, 1996.
[93] I.P. Evans, A. Spencer, G. Wilkinson, J. Chem. Soc. Dalton Trans. (1973) 204–209.
[94] E. Terpetschnig, J.D. Dattelbaum, H. Szmacinski, J.R. Lakowicz, Anal. Biochem. 251 (1997) 241–245.
[95] H.G. Suresh, A.X. da Silveira Dos Santos, W. Kukulski, J. Tyedmers, H. Riezman, B. Bukau, A. Mogk, Mol. Biol. Cell 26 (2015) 1601–1615.
[96] L. Sandager, M.H. Gustavsson, U. Stahl, A. Dahlqvist, E. Wiberg, A. Banas, M. Lenman, H. Ronne, S. Stymne, J. Biol. Chem. 277 (2002) 6478–6482.
[97] H. Ito, Y. Fukuda, K. Murata, A. Kimura, J. Bacteriol. 153 (1983) 163–168.
[98] APEX2 v2012.4, Bruker AXS, Madison, WI, 1999.
[99] N. Walker, D. Stuart, Acta Crystallogr., Sect. A 39 (1983) 158–166.
[100] G.M. Sheldrick, SADABS, Area Detector Absorption Correction, University of Göttingen, Göttingen, Germany, 2001.
[101] G.M. Sheldrick, SHELX-97, Program for Refinement of Crystal Structures, University of Göttingen, Göttingen, Germany, 1997.
[102] L.J. Farrugia, WINGX ver. 1.70, An Integrated System of Windows Programs for the Solution, Refinement, and Analysis of Single Crystal X-ray Diffraction Data, Department of Chemistry, University of Glasgow, 2005.
[103] G.M. Sheldrick, Acta Crystallogr. Sect. A 64 (2008) 112–122.
[104] M.N. Burnett, C.K. Johnson, ORTEP-III, Report ORNL – 6895, Oak Ridge National Laboratory, Oak Ridge, TN, 1996.
[105] J. Marmur, J. Mol. Biol. 3 (1961) 208–218.
[106] M.F. Reichmann, S.A. Rice, C.A. Thomas, P. Doty, J. Am. Chem. Soc. 76 (1954) 3047–3053.
[107] A. Wolfe, G.H. Shimer, T. Meehan, Biochemistry 26 (1987) 6392–6396.
[108] M. Lee, A.L. Rhodes, M.D. Wyatt, S. Forrow, J.A. Hartley, Biochemistry 32 (1993) 4237–4245.
[109] J.R. Lakowicz, Principles of Fluorescence Spectroscopy, 3rd ed., Springer, New York, 2006.
[110] G. Scatchard, Ann. N. Y. Acad. Sci. 51 (1949) 660–672.
[111] J. Tang, F. Luan, X. Chen, Bioorg. Med. Chem. 14 (2006) 3210–3217.
[112] G.K. Azad, V. Singh, P. Mandal, P. Singh, U. Golla, S. Baranwal, S. Chauhan, R.S. Tomar, FEBS Open Bio 4 (2014) 77–89.
[113] A. Pidoux, B. Mellone, R. Allshire, Methods 33 (2004) 252–259.